

Lawrence Berkeley National Laboratory

LBL Publications

Title

Quantifying Site Effects and Their Influence on Earthquake Source Parameter Estimations Using a Dense Array in Oklahoma

Permalink

<https://escholarship.org/uc/item/8jm0n4tr>

Journal

Journal of Geophysical Research: Solid Earth, 128(9)

ISSN

2169-9313

Authors

Chang, Hilary
Abercrombie, Rachel E
Nakata, Nori
[et al.](#)

Publication Date

2023-09-01

DOI

10.1029/2023jb027144

Copyright Information

This work is made available under the terms of a Creative Commons Attribution-NonCommercial License, available at <https://creativecommons.org/licenses/by-nc/4.0/>

Peer reviewed

JGR Solid Earth

RESEARCH ARTICLE

10.1029/2023JB027144

Key Points:

- Alluvial sediments increase vertical ground motions by up to a factor of 3.5 in the 40 km by 23 km study region
- Local site conditions in a low-relief river plain have a systematic influence on source parameters characterized by individual spectra
- Even for small earthquakes, complex sources can cause large variability in source parameters

Supporting Information:

Supporting Information may be found in the online version of this article.

Correspondence to:

H. Chang,
hilarych@mit.edu

Citation:

Chang, H., Abercrombie, R. E., Nakata, N., Pennington, C. N., Kemna, K. B., Cochran, E. S., & Harrington, R. M. (2023). Quantifying site effects and their influence on earthquake source parameter estimations using a dense array in Oklahoma. *Journal of Geophysical Research: Solid Earth*, 128, e2023JB027144. <https://doi.org/10.1029/2023JB027144>

Received 24 MAY 2023

Accepted 29 AUG 2023

Author Contributions:

Conceptualization: Hilary Chang, Rachel E. Abercrombie, Nori Nakata, Colin N. Pennington
Data curation: Hilary Chang, Kilian B. Kemna, Elizabeth S. Cochran, Rebecca M. Harrington
Formal analysis: Hilary Chang
Funding acquisition: Rachel E. Abercrombie, Nori Nakata
Investigation: Hilary Chang
Methodology: Hilary Chang, Rachel E. Abercrombie, Nori Nakata

© 2023 The Authors.

This is an open access article under the terms of the [Creative Commons Attribution-NonCommercial License](https://creativecommons.org/licenses/by-nc/4.0/), which permits use, distribution and reproduction in any medium, provided the original work is properly cited and is not used for commercial purposes.

Quantifying Site Effects and Their Influence on Earthquake Source Parameter Estimations Using a Dense Array in Oklahoma

Hilary Chang¹ , Rachel E. Abercrombie² , Nori Nakata^{1,3}, Colin N. Pennington⁴, Kilian B. Kemna⁵ , Elizabeth S. Cochran⁶ , and Rebecca M. Harrington⁵

¹Department of Earth, Atmospheric, and Planetary Sciences, Massachusetts Institute of Technology, Cambridge, MA, USA,

²Department of Earth and Environment, Boston University, Boston, MA, USA, ³Lawrence Berkeley National Laboratory, Berkeley, CA, USA, ⁴Lawrence Livermore National Laboratory, Livermore, CA, USA, ⁵Ruhr University Bochum, Bochum, Germany, ⁶U.S. Geological Survey, Earthquake Science Center, Pasadena, CA, USA

Abstract We investigate the effects of site response on source parameter estimates using earthquakes recorded by the LArge-n Seismic Survey in Oklahoma (LASSO). While it is well known that near-surface unconsolidated sediments can cause an apparent breakdown of earthquake self-similarity, the influence of laterally varying site conditions remains unclear. We analyze site conditions across the 1825-station array on a river plain within an area of 40 km by 23 km using vertical ground motions from 14 regional earthquakes. While the source radiation pattern controls P-wave ground motions below 8 Hz, the surface geology correlates with P-wave ground motions above 8 Hz and S-wave ground motions at 2–21 Hz. Stations installed in alluvial sediments have vertical ground motions that can exceed three times the array median. We use the variation of ground motion of regional earthquakes across the array as a proxy for site effects. The corner frequencies and stress drops of local earthquakes ($M_L = 0.01$ –3) estimated using a standard single-spectra approach show negative correlations with the site-effect proxy, while the seismic moments show positive correlations. In contrast, the spectral-ratio approach effectively shows no correlation. The overall bias is small as expected for this relatively homogeneous structure; accurate estimation of site-related biases requires at least 30 stations. Correcting for site-related biases reduces the standard deviations of the source parameters by less than 13% of the total variations. Remaining variations are partially associated with source directivity and model misfits— as small earthquakes can have complex ruptures.

Plain Language Summary An observed earthquake record is affected by the earthquake source, the wave path, and local site conditions, such as geology and soil properties. We need to separate these terms to accurately characterize the earthquake source. However, how local site conditions, called site effects, affect our ability to estimate accurate source parameters is not well-understood. We use a dense array in Oklahoma on a flat river plain to quantify the influence of site effects on previously estimated source parameters, including corner frequency, seismic moment, and stress drop. The ground motions from regional earthquakes can be three times larger in certain frequency bands and time windows with spatial patterns that are related to the geology. We use the ground motions as a proxy for relative site effects. Despite the small structural changes, site effects systematically influence source parameters estimated using a standard approach of fitting individual spectra. In comparison, the spectral-ratio approach that uses co-located event pairs effectively removes site effects. We recommend a minimum of 30 stations to capture the site effects. In addition to the systematic site-effect related bias, observations made by single stations are subject to large uncertainty associated with source directivity and complex rupture, even for small earthquakes.

1. Introduction

An earthquake seismogram is a combination of source, path, and site effects. In the frequency domain, the earthquake displacement spectrum $u(f)$ can be expressed by (Boore, 2003):

$$u(f) = e(f)p(f)s(f), \quad (1)$$

where f is the frequency, $e(f)$ is the source spectrum, $p(f)$ is the influence of the wave path, and $s(f)$ represents the site effect caused by near surface heterogeneity. The site effect $s(f)$ has been of great interest for earthquake

Project Administration: Rachel E. Abercrombie, Nori Nakata
Resources: Nori Nakata
Software: Hilary Chang, Rachel E. Abercrombie, Kilian B. Kemna
Supervision: Rachel E. Abercrombie, Nori Nakata
Validation: Hilary Chang
Visualization: Hilary Chang
Writing – original draft: Hilary Chang
Writing – review & editing: Hilary Chang, Rachel E. Abercrombie, Nori Nakata, Colin N. Pennington, Kilian B. Kemna, Elizabeth S. Cochran, Rebecca M. Harrington

engineering, as soft, unconsolidated sediments can cause significant amplification of ground motion, or resonance (Borcherdt, 1970; Field et al., 1997). Ground motion prediction models aim to characterize site responses using ground motion observations (e.g., the horizontal-to-vertical noise spectral ratio (H/V ratio); Nakamura, 1989), rock and soil properties such as shear-wave velocity (Boore et al., 1993; Borcherdt, 1994) and attenuation (e.g., Anderson & Hough, 1984; Ktenidou et al., 2014), and topography (Wald & Allen, 2007; Yong et al., 2012). Ground Motion Prediction Equations (GMPEs) use the so-called V_{s30} , or the averaged shear-wave velocity over the top 30 m, as a proxy for site effects (Boore et al., 2014; Goulet et al., 2018). Wald and Allen (2007) and Yong et al. (2012) estimate V_{s30} using the slope and convexity of the topography to characterize site conditions. In the Central and Eastern United States (U.S.) where large post-glacial sedimentary basins overlay stable cratons, the depth to the crystalline basement also plays an important role in ground motion modeling (Goulet et al., 2018).

Site effects result in biases when we try to measure earthquake source parameters from the source spectra $e(f)$. The source parameters, including corner frequency, seismic moment, and stress drop, are important for understanding the size of the rupture and the energy being released. However, derived earthquake source parameters suffer from large uncertainties that can vary across several orders of magnitude, of which the cause is still poorly resolved (Abercrombie, 2021; Allmann & Shearer, 2009; Kane et al., 2011; Pennington et al., 2021; Taira et al., 2021). Shallow geologic structure that amplifies some frequencies while highly attenuating others can bias corner frequency and stress drop estimates (e.g., Abercrombie, 1995; Ko et al., 2012). It is still not clear how much lateral site heterogeneity contributes to source parameter uncertainty. The influence of site effects is often buried in the large uncertainty due to model misfits caused by using an overly simplistic source model to fit complex source spectra (Abercrombie, 2021; Kaneko & Shearer, 2014, 2015). In this study, we use the spatially dense data from the LARge-n Seismic Survey in Oklahoma (LASSO) (Dougherty et al., 2019) to investigate the uncertainties of source parameters and the influence of site effects. The relatively homogeneous structure in the region (low relief, near-horizontal sedimentary structure) allows us to assess the influence of site effects when relatively little variation would typically be expected.

An earthquake source is typically modeled using a simple circular rupture and parameters including corner frequency (f_c), seismic moment (M_0), and stress drop ($\Delta\sigma$), that are related to the dimension, size, and energy released from the source. Source parameters can be estimated by modeling the far-field source displacement spectrum $\Omega_t(f)$ (Boatwright, 1978; Brune, 1970):

$$\Omega_t(f) = \frac{\Omega_0 e^{-(\pi f t/Q)}}{[1 + (f/f_c)^n]^{1/\gamma}}, \quad (2)$$

where Ω_0 is the long-period spectral amplitude, t is travel time, n is the high frequency fall-off rate, Q is the frequency-independent quality factor, and γ controls the shape of the corner depending on whether a Brune ($\gamma = 1$; Brune, 1970) or a Boatwright ($\gamma = 2$; Boatwright, 1980) model is used. After fitting Equation 2 to estimate f_c and Ω_0 , the seismic moment is determined by (Shearer, 2019):

$$M_0 = \frac{4\pi\rho c^3 R\Omega_0}{U_{\phi\theta}}, \quad (3)$$

where ρ is the rock density, c is the P-wave velocity at the focal depth, R is the hypocentral distance, and $U_{\phi\theta} = 0.52$ is the mean radiation pattern coefficient for P waves (Boore & Boatwright, 1984). The use of a constant $U_{\phi\theta}$ may not fully account for the influence of the radiation pattern. If we assume a theoretical rupture model (Madariaga, 1976), the uniform stress drop across a circular crack can be expressed by (Eshelby, 1957):

$$\Delta\sigma = \frac{7}{16} \left(\frac{f_c}{k\beta} \right)^3 M_0, \quad (4)$$

where k is a constant related to the spherical average of the model corner frequency. The shear wave velocity at the source focal depth is represented by β . A constant stress drop implies earthquake self-similarity, where corner frequency scales inversely with seismic moment in Equation 4. Stress drop uncertainties remain largely unconstrained and the calculated stress drop values among different studies can vary across several magnitudes (Abercrombie, 2021). The main source of uncertainty rests in the f_c estimate, which is amplified through the cubic relation in Equation 4. As mentioned previously, non-source related effects can cause scatter in f_c . While

attenuation along the path is included in the model by assuming frequency-independent Q in Equation 2, site effects are more difficult to estimate.

The LASSO array was deployed between 14 April and 10 May in 2016 to record local earthquakes likely induced by saltwater disposal (Dougherty et al., 2019). The saltwater, which is a byproduct of oil and gas production, was injected into 1–2 km deep injection wells. LASSO consisted of 1,825 stations in a 40 km by 23 km region (spacing ~ 400 m) of little topographic relief. The region has horizontally layered sedimentary rocks of Permian and Quaternary ages overlaid by alluvial sediments and terrace deposits from streams and rivers (Heran et al., 2003). More than a thousand local events were recorded during the 26-day deployment period (Cochran, Wickham-Piotrowski, et al., 2020). By comparison, a typical regional network or temporary deployment would likely have one to five stations deployed in a region of similar size (e.g., Cochran, Wolin, et al., 2020; Hauksson et al., 2020), making it hard to distinguish source, path and site effects. Kemna et al. (2020) investigated the source properties of events recorded by LASSO, including corner frequency, seismic moment, and stress drop. They found that source parameter estimates vary significantly across the array (relative deviation as high as 150% for measurements made by < 5 stations) and statistically quantified the expected deviation with increasing number of stations. Here, we attempt to quantify the contribution of site effects to the variability of source parameters estimates calculated using (a) a standard approaches by fitting earthquake source spectra and (b) a spectral-ratio method (Hartzell, 1978; Hough, 1997). Spectral-ratio approaches in which one or more small, co-located earthquakes are used to remove or reduce the influence of the path and site and isolate the source are commonly preferred (Abercrombie, 2014; Huang et al., 2017; Ko et al., 2012; Kwiatek et al., 2014; Mori & Frankel, 1990; Shearer et al., 2006; Viegas et al., 2010), when suitable small earthquake recordings are available. We apply the spectral-ratio approach to a small number of events to see if the spectral-ratio approach reduces the source parameter variability.

In the following, we first introduce the LASSO array and the data set. We then divide the analyses into four sections: we start by evaluating and quantifying the site conditions across the array using ground motion from regional earthquakes. Then, we derive an empirical relation between our estimated site effects and source parameter estimates of local earthquakes, comparing the standard single-spectra approach and a spectral-ratio approach. Next, we use this relation to correct the measured source parameters and estimate the influence of site effects. Finally, we discuss the implications for the variability of source parameters.

2. Data and the LASSO Array

The LARge-n Seismic Survey in Oklahoma (LASSO; Figure 1) operated for a month in 2016. The array consisted of 1,825 vertical-component nodal geophones with an inter-station spacing of ~ 400 m (Dougherty et al., 2019). The nodal geophones have a resonance frequency of 10 Hz and a sampling rate of 500 Hz. The array covered an area of 40 km by 23 km with maximum elevation difference of less than 150 m (Figure 2a). The small topographic relief predicts V_{s30} values ranging from 200 to 500 m/s based on a topographic slope V_{s30} model from Wald and Allen (2007). The range of V_{s30} matches the dense (CD)—loose sand (DE) categories in the site classification defined by the National Earthquake Hazards Reduction Program (NEHRP) (Figure S1b in the Supporting Information S1; Building Seismic Safety Council, 2020). The Salt Fork Arkansas River that passes through the southern third of the array is fed by the stream systems to the south and north (Figure 2a) and the Great Salt Plains Lake to the west. The regional geological structure (Figure 2b) consists of combinations of shale, siltstone, sandstone, and conglomerate of Permian age with no significant folding or faulting, overlain in places by Quaternary alluvium and terrace deposits (Heran et al., 2003). Quaternary unit thickness in Oklahoma ranges from 8–30 m (Johnson & Luza, 2008). The depth to the Precambrian crystalline basement is 2.5 km, dipping $< 1^\circ$ to the south-west (Crain & Chang, 2018). The sparsely populated area has one main East-West oriented state highway that passes through the middle of the array. The raw data were recorded in vertical velocity. We demean, detrend, prefilter (bandpass between 0.006 and 250 Hz), remove the instrument response, and convert the data to displacement (Text S1 in the Supporting Information S1).

The LASSO array recorded 1,104 events with local magnitudes (M_L) ranging from 0.01 to 3.0 (Cochran, Wickham-Piotrowski, et al., 2020) that occurred primarily between 1.5 and 5.5 km depth. Kemna et al. (2020) calculated corner frequency, seismic moment, and static stress drop from P-wave spectra for a total of 962 events, of which they investigate the estimate robustness of 336 events. They found that stress drop values scatter (with relative deviation of 30% within a 95% confidence interval) even when using as few as 20 stations. The seismic

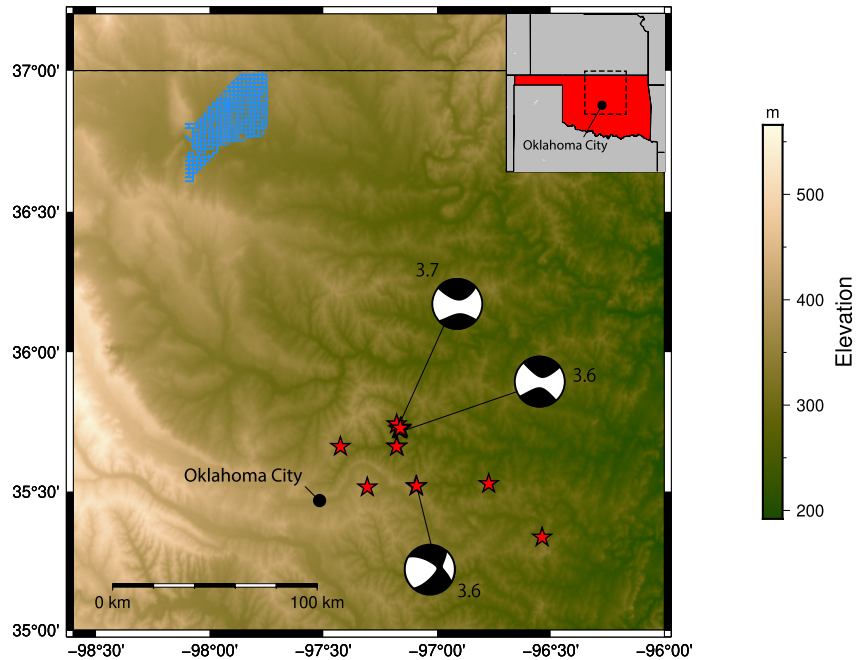


Figure 1. Location of the LARge-n Seismic Survey in Oklahoma array (blue dots) and 14 regional events (M_L or $M_{wr} = 3.0$ – 3.7 ; Table S1 in the Supporting Information S1) used to quantify site effects (red stars, with some stars overlapping). Upper right inset shows the array location (dashed square) in Oklahoma (shaded in red). Focal mechanisms and magnitudes are shown for the three largest events (U.S. Geological Survey, 2022). The back-azimuth ranges from 143° to 161° . The elevation data are from NASA JPL (2013).

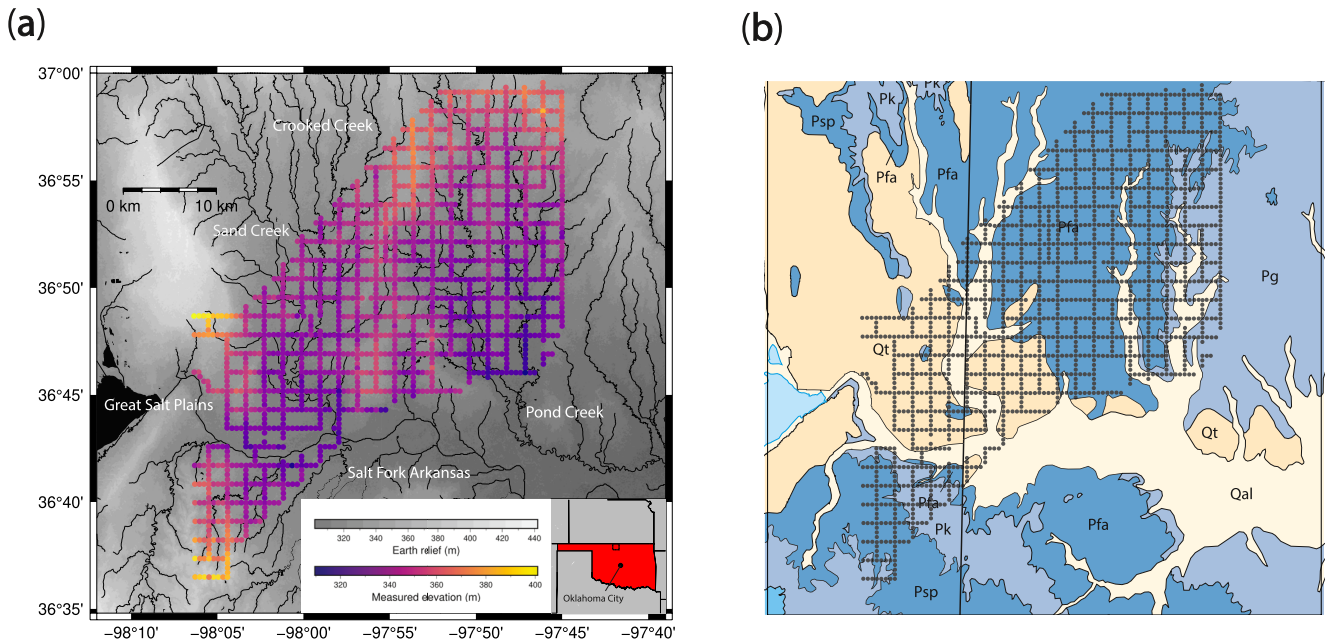


Figure 2. Topography (a) and geological units (b) near the LARge-n Seismic Survey in Oklahoma (LASSO) array. The black networks (a) are stream systems (Oklahoma Water Resources Board, 2022) with relief shown in gray scale (NASA JPL, 2013). Colored dots show the elevation at LASSO stations. Inset on the bottom right shows the array location (black box) in Oklahoma (shaded in red). In (b), the geological units in yellow colors (Qal, Qt) are Quaternary alluvium (Qal, age: Holocene) and terrace deposits (Qt, age: Pleistocene) (Heran et al., 2003). The youngest unit, Qal, hosts the riverbeds of the main stream systems in (a). The units in blue (Pk, Psp, Pfa, Pg) are of Permian age. Pk and Psp contain combinations of shale, siltstone, and sandstone; Pfa is mainly shale; Pg is mainly sandstone and conglomerate. The cyan color block is the Great Salt Plains Lake. Black dots mark LASSO stations. The map on the left and right of the vertical line are from two reports compiled in Heran et al. (2003).

moment and corner frequency estimates from individual spectra exhibit spatially coherent patterns across the array (Figure 2 in Kemna et al., 2020). The reason for the large variation was not clear and may result from source, site effects, or uncertainties in the measurement. Trugman et al. (2021) suggested these events have complicated source mechanisms based on the decreasing double-couple component of the P-wave radiation patterns, particularly at frequencies above 15 Hz. Pennington et al. (2022) investigated several small magnitude events and found they have complicated source-time-functions that deviate from a simple pulse and suggest complex ruptures. They were able to map the heterogeneous slip distributions using finite fault inversion. Source complexity can increase the uncertainty of source parameters when estimated assuming a simplified spectral model such as Equation 2 (Abercrombie, 2021). Building on these studies, we quantify the contribution of site effects to the variability of source parameters reported in Kemna et al. (2020).

3. Quantifying Site Effects

3.1. Method

To use the ground motions of reference earthquakes as a proxy for site effects, reference earthquakes must meet two requirements. The first requirement is that there should be minimal variations across the array caused by path and source effects. The second requirement is the availability of higher frequency signals, ideally, above 4 Hz (Al-Shukri et al., 1995), to characterize near-surface site conditions in the same frequency range that is used to model source parameters. The earthquakes that best meet the first requirement are teleseismic earthquakes (>1,000 km), but the signal bandwidths of teleseismic events are generally below 1 Hz. Hence, we follow Johnson et al. (2020) and use the ground motion of regional events to investigate site response. We use 14 regional earthquakes (regional magnitude M_{wr} or local magnitude $M_L = 3.0$ –3.7) in Central Oklahoma (red stars in Figure 1; Text S2 in the Supporting Information S1). The hypocentral distances are approximately 140–240 km, which are about 2.7–4.6 times the array aperture (40 km). The spectrograms have clear P- and S-arrivals (Figure S2 in the Supporting Information S1). The majority of the stations have signal-to-noise ratio (SNR) between 3 and 250 over the 2–21 Hz range (except for the P waves of the smallest event).

We calculate the root-mean-square (RMS) amplitude of vertical ground displacement of the 14 regional earthquakes across a range of frequency bands and time windows. The nine frequency bands that we examine are 0.5–1 Hz, 1–2 Hz, 2–4 Hz, 4–6 Hz, 6–8 Hz, 8–10 Hz, 10–15 Hz, 15–21 Hz, and 21–27 Hz. The five time windows relative to P-arrival times (phase arrivals) that we investigate are: –1–10 s (P-arrival and P-coda), 3–13 s (P-coda), 10–30 s (S-arrival and S-coda), 25–35 s (S-coda), and –1–30 s (both P-, S-arrivals and their coda). We pick the P-arrivals by visually examining the moveout across the array assuming the P-wave velocity (v_p) is constant (we find $v_p = 6.46$ km/s). The S waves arrive between 17–19 s after the P waves. We calculate the background noise level by the RMS amplitudes in a window before the P-arrival (–50 to –20 s). The background noise level is small compared to the P and S waves at most of the stations (SNR >3) (Figure S3 in the Supporting Information S1). We subtract the noise level from the median RMS amplitude to use only earthquake-related ground motions.

Because of the size of the LASSO array, we first need to minimize the ground motion amplitude variations that may be attributed to path effects. Path effects are related to source-station distances and result from geometric spreading and attenuation. We apply a least squares regression method similar to Trugman et al. (2021) to remove the travel-time (i.e., distance) dependent trends (Text S3 in the Supporting Information S1). The path-effect adjustments are small, confirming the regional earthquakes are sufficiently far from the array and that site effects likely dominate the variability (Figure S4 in the Supporting Information S1).

After adjusting for path effects, we calculate a “residual” term for each station to quantify the ground motion variability. We define the residual to be the deviation of the ground motion, $(dev(A))_i$, from the array median:

$$dev(A)_i = \frac{A_i - \bar{A}}{|\bar{A}|}, \quad (5)$$

where, for each frequency band, A_i is the median RMS amplitude of the 14 events at station i and \bar{A} is the median RMS amplitude of the 14 events across all stations in the array. We call the residual term determined from Equation 5 the “site RMS” (the site-effect proxy) in the rest of the article. We also investigate using peak-ground-velocity (PGV) to quantify ground motions following Johnson et al. (2020). The RMS amplitude and the PGV have

similar deviation patterns across the array (Figures S5 and S6 in the Supporting Information S1), so using either the RMS amplitude or the PGV as the site effect proxy yields negligible differences in the following analysis.

We examine several site-specific parameters to determine their influence on ground motion variation, including: far-field radiation pattern, surface geology, hypocentral distance, and V_{s30} . The largest three regional events have focal mechanism solutions (U.S. Geological Survey, 2022). We use the far field function in Obspy (Beyreuther et al., 2010) to calculate the radiation pattern on the vertical component based on the focal mechanisms. We quantify the surface geology by upsampling (spacing 50 m) the digital map of Heran et al. (2003) and labeling Quaternary and Permian unit grid points with 1 and 0, respectively. At the boundaries of the two units, the thickness of the sedimentary rocks likely changes gradually. To account for the gradual change between units, we smooth the grid with a Gaussian filter with a standard deviation of ~ 0.5 km after assigning the labels. We then interpolate values at station locations as a rough quantification of surface geology. We interpolate the V_{s30} values directly at station locations on the V_{s30} digital map from Wald and Allen (2007). See Figure S1 in the Supporting Information S1 for the site-specific values we assign for geological units and V_{s30} .

We evaluate the correlation between the site RMS and the site-specific parameters using the Pearson's correlation coefficient (cc) and p-value. The cc is the degree of linear correlation between the data sets while the p-value indicates the statistical significance. We deem a p-value less than 0.05 to indicate significant correlation, in which the probability of an uncorrelated data set exhibiting a similar apparent correlation would be less than 5%.

3.2. Results

The site RMS values exhibit significant frequency and time-window dependence across the array (Figures 3a and 3b). The range of variability can reach 1–3.5 times the array median. The variability can be attributed to the source radiation pattern or the site effects. For the P waves (Figure 3a), the variability between 2 and 4 Hz is dominated by the source radiation pattern of the largest regional event (Figure 3c; Event 1 in Table S1 in the Supporting Information S1). The focal mechanisms of the three largest events have similar influence on the array (Figure S7 in the Supporting Information S1) because of consistent fault orientations in the source region (Holland, 2013). For the S waves (Figure 3b), the large amplifications (345%) between 2 and 4 Hz qualitatively correspond to the Quaternary unconsolidated sedimentary units (Qt, Qal). Amplification of the youngest alluvial unit (Qal) appears to have a significant impact on S-wave ground motions at all frequencies and P waves above 6 or 8 Hz (Figure 3d); the highest ground motions correlate with alluvial units along the major stream systems. An area of anomalous site RMS values occurs in the SW corner of the array where the geologic map indicates Permian units (Psp, Pk, and Pfa). The field crew that deployed the array indicated this area was notably sandy. These sandy deposits appear to be absent on the geological map, but the signature of unconsolidated sandy deposits is visible in the high frequency ground motion data.

To quantify the spatial patterns described above, we calculate cross correlation values between site RMS and site parameters. We observe a high correlation ($>0.6cc$) between P-wave radiation pattern and the site RMS at 2–4 Hz (Figure 4a left), confirming the strong influence of the radiation pattern. We find site RMS positively correlates with surface geology (the Quaternary units) across all frequency bands for S waves and above 8 Hz for P waves, with overall larger cc values between site RMS and surface geology for S waves at 2–4 Hz (Figure 4a right). The positive correlation agrees with the observations in Figure 3, where the amplification is concentrated at the youngest alluviums (Qal). Note that we cannot determine whether site RMS and surface geology correlate above 21 Hz due to inadequate SNR.

Hypocentral distance has a cc less than 0.1 with site RMS after removing path effects, with the exception of frequencies below 6 Hz in the P-wave window, which is likely due to coincidental correlation with the P-wave radiation pattern. The V_{s30} estimates based on topographic slope have low or insignificant cc with site RMS for all frequency bands and phase windows. The low correlation with topographic slope variations are presumably due to the roughly flat relief (<150 m elevation change in Figure 2a), such that the topographic slope variations are not a good proxy for local V_{s30} .

Note that we must interpret the cc carefully because some site parameters spatially correlate with each other and result in an apparent correlation with site RMS. For example, the Quaternary units are more abundant on the west side of the array (Figure 3d). Hence, the surface geology spatial pattern tends to be opposite to the P-wave radiation pattern and is similar to the S-wave radiation pattern (Figures 3c and 3d). For P waves, the negative cc between the low-frequency site RMS and surface geology, and between high-frequency site RMS and radiation patterns, are

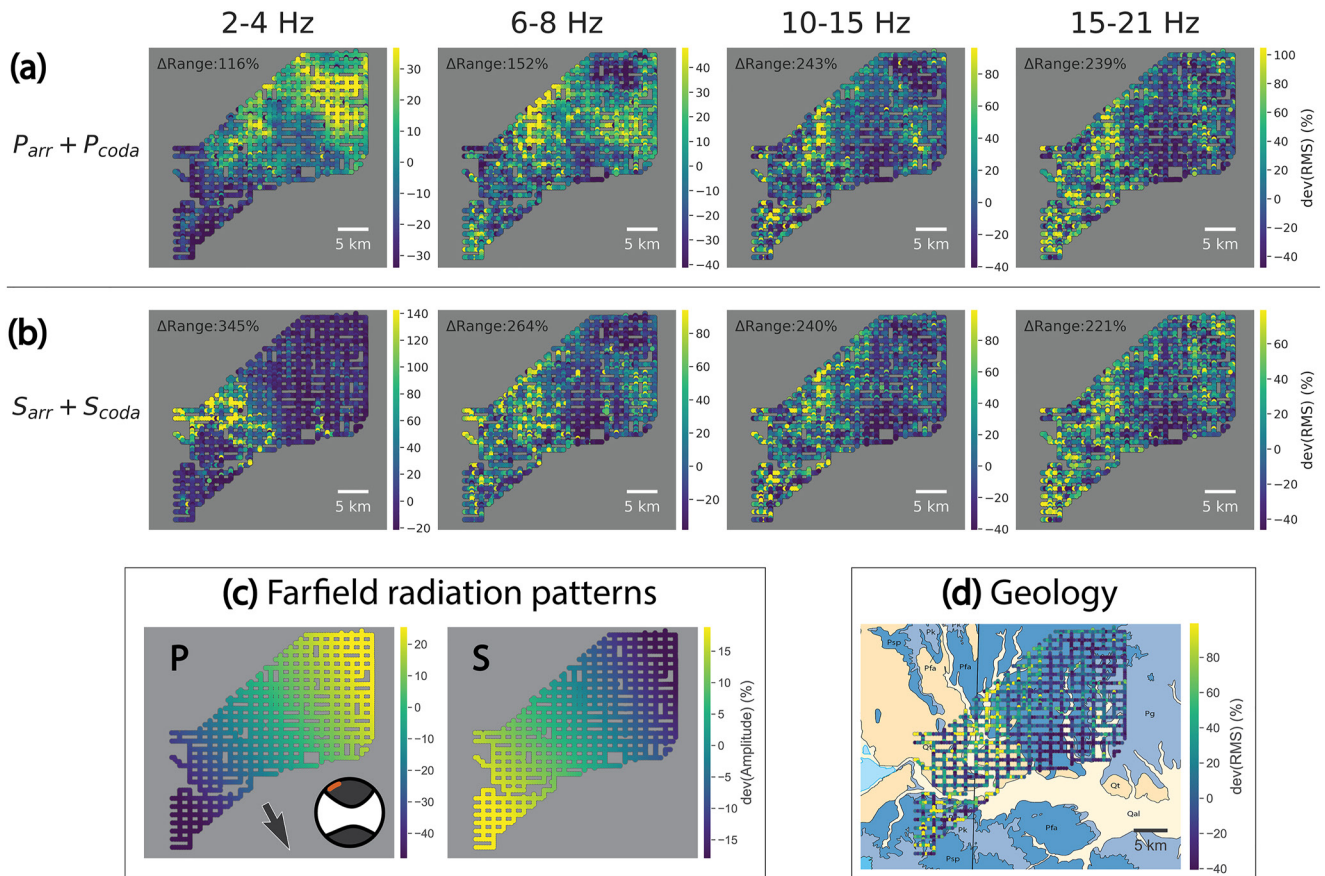


Figure 3. Site residuals (site RMS) quantified by the median Root-Mean-Square (RMS) amplitudes of 14 regional earthquakes in the (a) P- and (b) S-wave windows with increasing frequency from left to right. The path effects are removed. Δ Range is the range of the site residuals (the difference between the lowest and the highest site RMS values excluding the extreme 1% on both side), which shows the ground motions can be 1.2 to 3.5 times the array median. The colorbar ranges are saturated to the lowest and highest 5% of the site RMS to emphasize spatial patterns. The patterns in (a) and (b) have apparent influence from (c) P- and S-radiation patterns and (d) local geology. (c) Shows the calculated far-field radiation patterns (vertical component) for the largest event (U.S. Geological Survey, 2022). The location of LARge-n Seismic Survey in Oklahoma array is indicated in red on the focal mechanism. The arrow indicates the back azimuth. In (d), sites in Quaternary units (Qal, Qt: pale yellow/yellow; Heran et al., 2003) tend to have higher RMS amplitudes (at 10–15 Hz in the S-wave window).

also likely to be only apparent correlations. Similarly, the influence of S-wave radiation pattern and geology are difficult to untangle because they positively correlate with each other. However, the S-wave radiation pattern is a weaker control on observed amplitudes because only vertical component data are available (Figure 3c).

For now, we choose the 10–15 Hz site RMS in the S-wave window ($S_{arr} + S_{coda}$) as a proxy for site effects because of the observed correlation with surface geology and the higher overall SNR of regional S waves compared to P waves (Figure 4b). Next, we examine whether this site effect proxy can be used to improve the coherency of stress drop and reduce the variability of source parameters for local earthquakes. In Section 5, we will compare how site RMS estimated for other frequency bands and time windows impact source parameter estimates.

4. Correlation Between Earthquake Source Parameters and Site RMS

We examine if source parameters (corner frequency, moment, and stress drop) correlate with site RMS. We examine corner frequency calculated by two different approaches: the single-spectral fitting method introduced in Section 1 (using measurements from Kemna et al., 2020), and the spectral-ratio method (Hartzell, 1978; Hough, 1997) that may more effectively remove site effects.

4.1. Methods: Single-Spectral Versus Spectral-Ratio Fitting

The first approach — the single-spectral fitting method — fits earthquake displacement spectra using Equation 2. The path effect is considered with an exponential term in the numerator that accounts for attenuation and travel

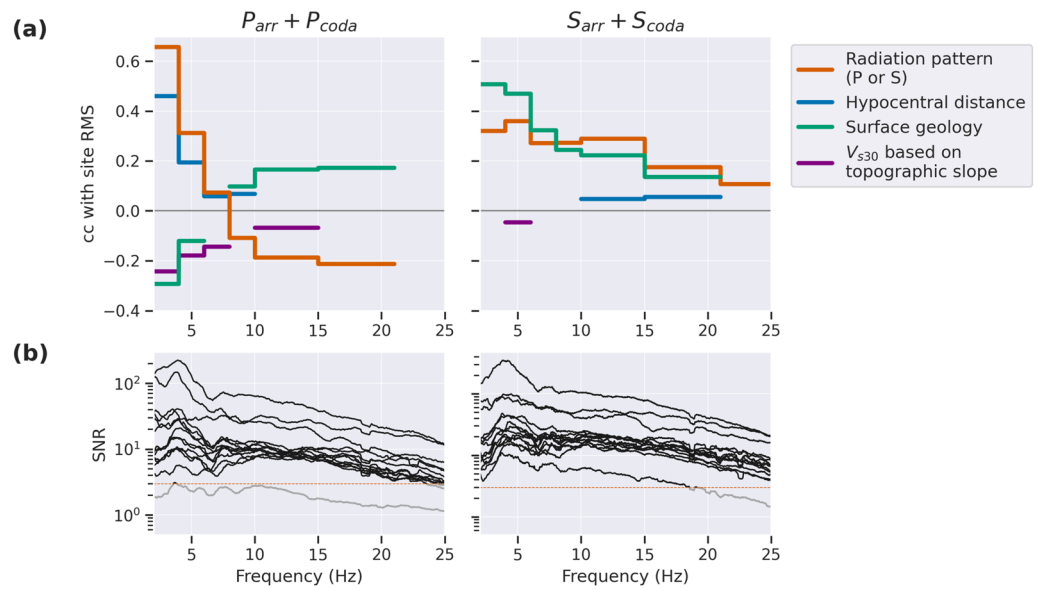


Figure 4. (a) Correlation coefficients (cc) between site parameters (see legend for color codes) and site root-mean-square (RMS) calculated for the P- (left column) and S-wave windows (right column) across a range of frequencies. We only show significant results (p -value < 0.05). The P-wave radiation pattern (red) dominates below 6 Hz and the surface geology (green) dominates at above 8 Hz. Note that the radiation pattern mirrors the geology, causing apparent correlations for both P and S waves (e.g., The higher cc between S-wave radiation pattern and site RMS above 10 Hz; see text for details). (b) The median signal-to-noise ratio (SNR) for each of the 14 regional events used to calculate site RMS. Only data with the median SNR > 3 (black curves above the dashed line) are included in the calculation.

time. Variations in the spectral falloff due to site effects are left uncorrected. Some approaches do solve for a high frequency attenuation term to account for shallow attenuation (Anderson & Hough, 1984; Kilb et al., 2012; Neighbors et al., 2017), but near surface amplification and resonance are still hard to quantify and constrain. We use the single-spectral fitting results from Kemna et al. (2020). We do not derive the uncertainties of the measurements.

For the second approach, the spectral-ratio method, we fit the ratio of the spectra of the main event and a co-located small event at individual stations to determine the corner frequency and moment (Hartzell, 1978; Hough, 1997). The spectral ratio at each station is

$$\Omega_r(f) = \Omega_{0r} \left[\frac{1 + (f/f_{c2})^\gamma}{1 + (f/f_{c1})^\gamma} \right]^{1/\gamma}, \quad (6)$$

where f_{c1} and f_{c2} are corner frequencies for the main and the small events, respectively, Ω_{0r} is the relative long-period spectral amplitude, and n and γ are the spectral fall-off rate, similar to Equation 2. The small event acts as an empirical Green's function (EGF) for the main event. By taking the ratio of the displacement spectra of a co-located event pair, the path and site effects are canceled, leaving only the source terms (Equation 1). Hence, we expect the spectral-ratio method to be less subject to site effects than the single-spectra modeling of Kemna et al. (2020).

We calculate spectral-ratios and estimate corner frequency at each station for three event pairs with local magnitudes between 2.1–2.5 (Table S2 in the Supporting Information S1) selected by Kemna et al. (2020), as the individual station measurements were not calculated in the earlier study. The corresponding EGF events have local magnitudes ranging between 1.1–1.4. The pre-analysis data treatments are similar to Section 3.1 (see Text S1 in the Supporting Information S1 for more details). We cut the time window 0.2 s before and 0.3 s after the P-arrivals and align the main event and EGF waveforms at their maximum correlation. Figure S8 in the Supporting Information S1 shows representative example spectra. We discard stations with poor quality data based on the following criteria (Abercrombie, 2014, 2015; Abercrombie et al., 2016): (a) the waveform correlation between main and EGF events must be > 0.7 ; (b) the longest continuous spectra must pass the SNR > 3

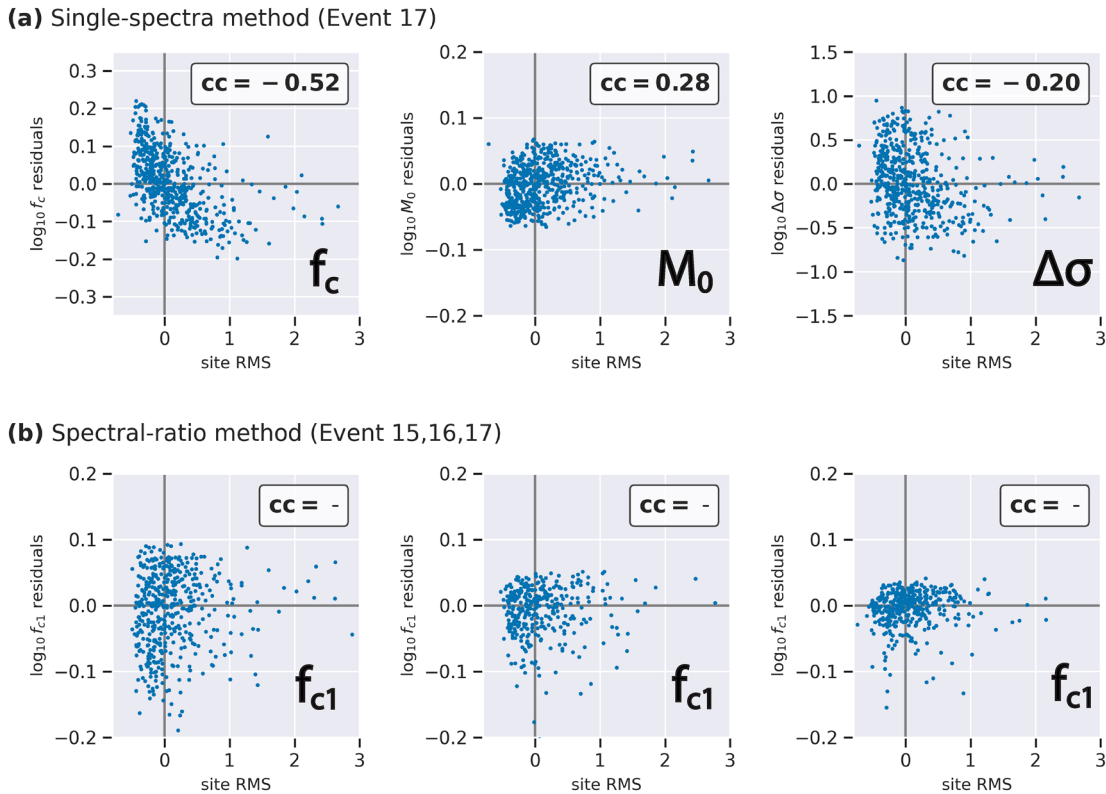


Figure 5. Correlation between site root-mean-square (RMS) and the residuals of source parameters (log-scaled) estimated using (a) single-spectral fitting method (number of samples (N) = 551 stations) and (b) spectral-ratio method (N = 385, 147, and 243 stations) at each station. Each dot is an individual station estimate. The origin is the median of the array. We only show cc values when they are significant (p -value < 0.05). “—” means insignificant. The site RMS are calculated in the S-wave time window (10–30 s) at 10–15 Hz. The source parameters estimated using single-spectra method have weak to moderate but significant bias related to site effects.

threshold in both main and EGF event for every frequency point; (c) the amplitude ratio (amp-ratio) between high- and low-frequency points on the best-fitted spectral-ratios model must be > 1.5 . This amp-ratio threshold is less strict than the amp-ratio > 2 used in Abercrombie (2014) enabling us to include more data; (d) to compensate for the less strict requirement, we discard the results if the standard fitting error is $> 20\%$. We first determine both f_{c1} and f_{c2} for the stacked spectral-ratio. We then determine the f_{c1} of individual ratios with f_{c2} fixed at the values determined by the stacked ratio. Fixing f_{c2} ensures the variation of f_{c1} is not related to changes in f_{c2} , which is often driven by fitting misfit (Shearer et al., 2019). Text S4 in the Supporting Information S1 provides additional details about the procedure.

We calculate the residuals of the (log-scaled) source parameters in a similar approach as shown in Equation 5 that is, $dev(\log_{10}f_c)$, $dev(\log_{10}M_0)$, and $dev(\log_{10}\Delta\sigma)$. Using the deviations allows us to minimize biases of individual events. We examine the cc between the source parameters and the site RMS and use a least squares regression method to determine the relation between them. We only use events recorded on at least 5 stations, and as many as 1,202 stations (906 total events). Because the source directivity can also contribute to the variability, we use the focal mechanism solutions in Trugman et al. (2021) (20 events) and calculate the distribution of cc between the P-wave radiation pattern, site RMS, and source parameters.

4.2. Results

The source parameters estimated using the single-spectral fitting method at each station correlate with site RMS at 10–15 Hz in the S-wave window (Figure 5a). The residuals of corner frequency and stress drop show a negative correlation while the moment shows a positive correlation with site RMS. The correlations, although weak, are significant. On the contrary, the corner frequencies estimated using spectral-ratio method show no such correlation (Figure 5b). The correlations suggest the single-spectral fitting method is more biased by site effects than the

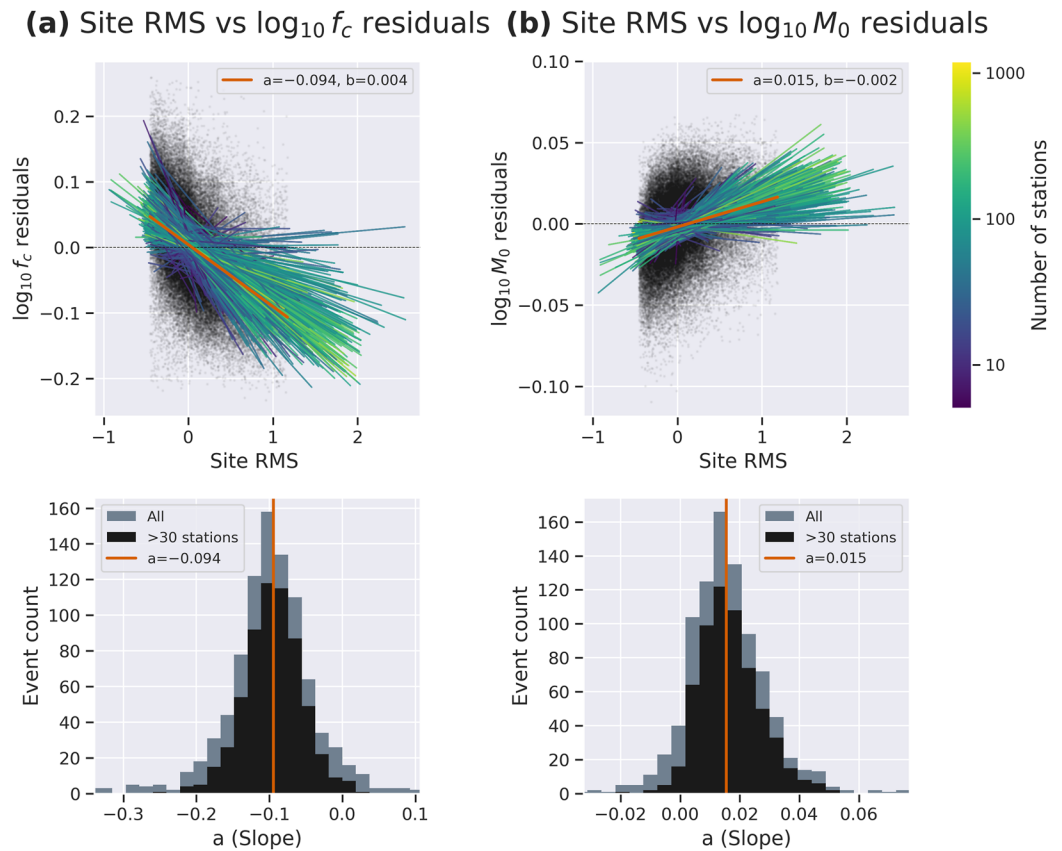


Figure 6. Estimated linear relations between site root-mean-square (RMS) and the residuals of log-scaled (a) f_c and (b) M_0 . We overlay the residuals of all individual station measurements from events with more than 5 stations as black dots in the top row (906 events in total; the maximum number of station is 1,202). The thin lines colored in yellow—purple are relations in individual events with the colors indicating number of available stations in each event (log-scaled). The thick red line is the average linear relation, with the slope (parameter a) and the y -intercept (parameter b) shown in the legend. The bottom panel shows the distributions of the slope (parameter a) center around the average relation (the red vertical line). Gray histograms show all events and black histograms show events with >30 stations. Site RMS is calculated in S-wave windows (10–30 s) at 10–15 Hz. The influence of site effects, being event-invariant, is consistent among all events, while event with >30 recordings is more likely to have an estimate closer to the average relation.

spectral-ratio method, as expected. They also demonstrate the effectiveness of the spectral-ratio method at removing site effects. However, the source parameters estimated using both methods still exhibit significant scatter.

We find the observed correlations are consistent among events, which agrees with the expectation that site effects are event-invariant. In Figure 6, we plot the site RMS versus the residuals of log-scaled corner frequency and moment for all local events and the linear relations determined separately for each event. The corner frequency negatively correlates with site RMS (Figure 6a) whereas the moment positively correlates with site RMS (Figure 6b). The negative correlation between corner frequency and site RMS is likely caused by the imprint of higher attenuation due to soft sediments on the spectra (Abercrombie, 1995, 1997; Sonley et al., 2006). The attenuation suppresses high frequency amplitudes and increases the spectral fall-off rate, and hence, trades off with the measured corner frequency (Ko et al., 2012). The positive correlation between moment and site RMS may be because the amplification of soft sediment boosts the plateau of the displacement spectra, which results in larger moment estimates (due to a larger Ω_0 in Equation 2). The deviation of corner frequency is more sensitive to site RMS than that of the moment (an absolute median slope of 0.101 in Figure 6a versus 0.018 in Figure 6b), which suggests the corner frequency measurements are more sensitive to attenuation-related fitting bias. Based on Equation 4, we expect a related bias in stress drop (Figure 5a). Events recorded on more stations have a relationship closer to the overall average as compared to those recorded on fewer stations, which are more poorly constrained. The average slope does not change significantly if calculating only using events with >30 stations.

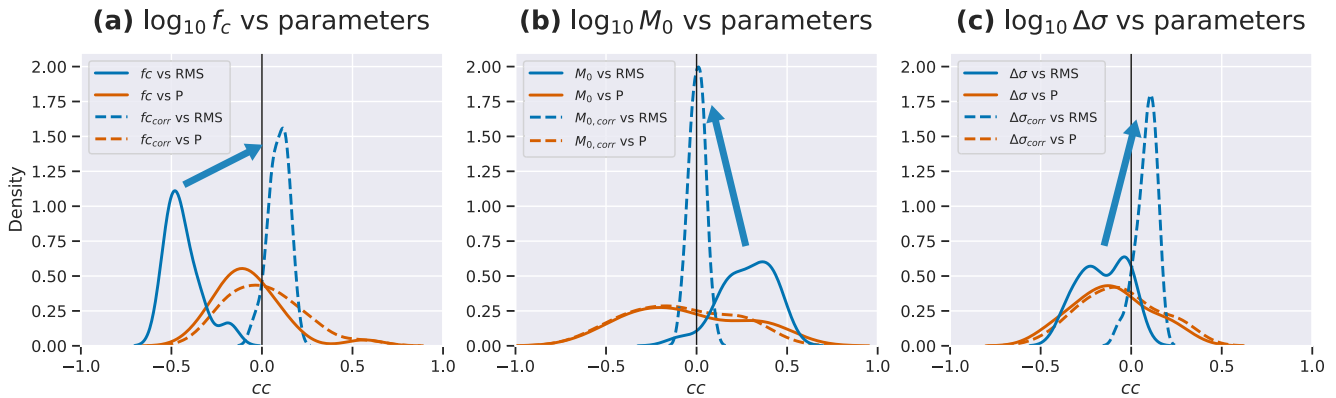


Figure 7. The kernel density distributions of correlation-coefficient (cc) of the residuals of (a) $\log_{10} f_c$, (b) $\log_{10} M_0$, and (c) $\log_{10} \Delta\sigma$ versus P-wave radiation pattern (red) or site root-mean-square (RMS) (blue). The solid curves show original data which shift to the dashed curves after the site-effect correction. Note the effective removal of the dependence on site effect (the distributions of cc are closer to 0, indicated by the arrows). The radiation pattern shows no obvious correlation with the source parameters (the distributions of cc center around 0) either before or after the site-effect correction. We calculate the radiation patterns using the focal mechanism solutions from Trugman et al. (2021) (20 local events). The site RMS is shown for the S-wave window (10–30 s) at 10–15 Hz.

The correlation coefficients between site RMS and the residuals of log-scaled f_c , M_0 , and $\Delta\sigma$ are narrowly distributed and center around -0.5 , 0.3 , and -0.1 , respectively (Figure 7; the solid curves in blue). The non-zero mean of the cc values demonstrates the site RMS causes a consistent bias in corner frequency, moment, and stress drop. In contrast, the distributions of cc between the P-wave radiation pattern and the source parameters (the solid curves in red) center around zero for this event. While the majority of events are similar, some events do show a large cc between the P-wave radiation patterns and source parameters, but these higher cc values are both positive or negative. Next, we use the site RMS to correct the source parameter estimates (dashed curves).

5. Applying Site-Effect Corrections to Source Parameters

5.1. Method

We apply an empirical correction to remove the trends in Figure 6 between site RMS and f_c and M_0 . For each event, the correction at station i is

$$cor_i = a \text{dev}(x)_i + b, \quad (7)$$

where x represents $\log_{10} f_c$ or $\log_{10} M_0$, $\text{dev}(x)_i$ is the residual of source parameter x at station i . a and b are the linear trend between $\text{dev}(x)$ and site RMS. Note that the corrections are not reliably estimated if an event has fewer than 30 stations (blue—purple lines in Figure 6); thus, it may not be feasible to apply this type of correction to a small network. We subtract the correction term from the source parameter residuals:

$$\text{dev}(x)_{cor,i} = \text{dev}(x)_i - cor_i. \quad (8)$$

We then determine the corrected f_c and M_0 :

$$x_{cor,i} = \text{dev}(x)_{cor,i} \times |\bar{x}| + \bar{x}, \quad (9)$$

where the \bar{x} in Equation 9 are the median value of $\log_{10} f_c$ or $\log_{10} M_0$ for all stations before the correction. We then recalculate stress drop using Equation 4 using the corrected f_c and M_0 values.

We next compare the effectiveness of the source parameter correction using site RMS at other frequencies and phase time windows. We examine the reduction of standard deviation of source parameters for all of the different site RMS corrections. The site-effect correction should be consistent from event to event at a given station, so we quantify the variability of the correction by computing the coefficient of variation:

$$CV = \text{inter-station median} \left[\frac{\text{inter-event standard deviation}(cor_i)}{\text{inter-event mean}(cor_i)} \right]. \quad (10)$$

where cor_i is the correction term at station i in Equation 7.

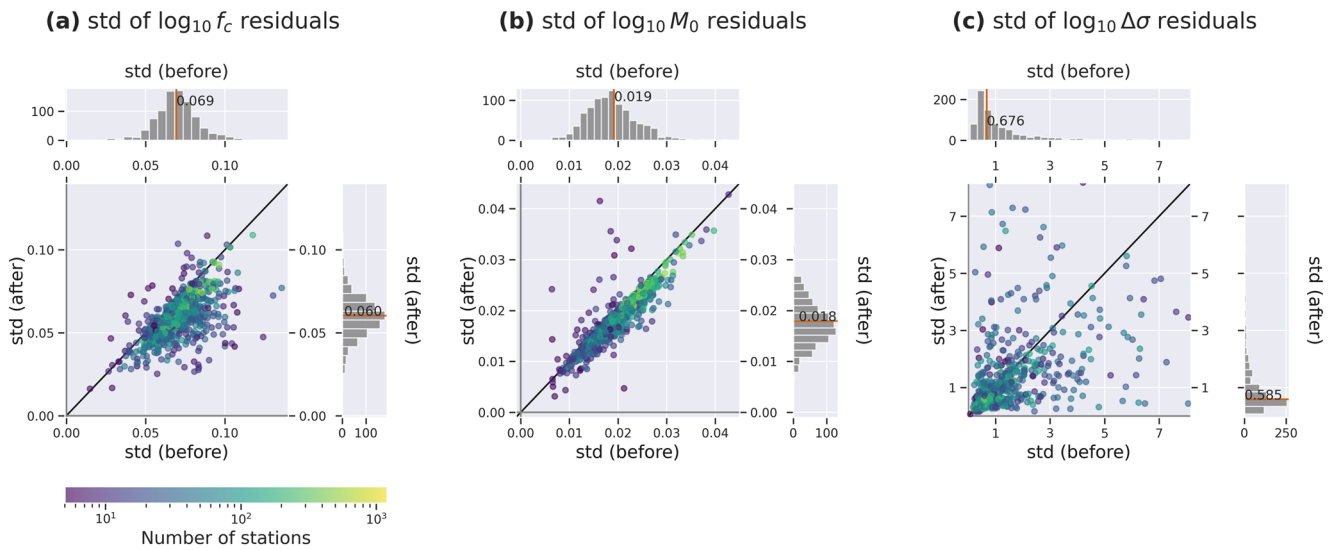


Figure 8. Source parameter variability for the 906 local events before and after the site-effect correction. Each dot is the standard deviation of the residuals of log-scaled (a) f_c , (b) M_0 , and (c) $\Delta\sigma$ estimates for an event before (x -axis) and after (y -axis) correction. Colors indicate the number of stations for each event and black lines are the 1:1 ratio. Histograms show the number of events along the x and y -axes, where the red lines are the median standard deviation for events with >30 stations. The correction uses site RMS in the S-wave window (10–30 s) at 10–15 Hz. The correction reduces the variability of the source parameters consistently for events with 30 or more stations (blue—green—yellow dots located below the 1:1 line).

To estimate the likely bias and variation caused by site effects for more typical network configurations with sparser station density, we use bootstrapping to consider randomly selected sub-arrays of the array. We calculate the reduction in the source parameter estimate deviation produced by the correction using small sub-arrays of LASSO nodes as a proxy for the expected uncertainty caused by site effects in a more typical source parameter study. We choose an event recorded on the highest number of stations (Event 1 with 1,202 recordings as shown in Table S1 of Kemna et al., 2020) and assume its median corner frequency, moment, and stress drop give the “true” values. We then randomly sample sub-arrays and calculate the median corner frequency, moment, and stress drop to investigate how sub-arrays may produce values that deviate from “true” median values. For sub-arrays with a given number of stations, we sample 100 times and take the median deviation for both original and corrected source parameters.

5.2. Results

The site-effect correction significantly reduces the correlation between source parameters and site RMS (the blue solid curves vs. the blue dashed curves in Figure 7). Nevertheless, small mean $cc > 1$ values remain between site RMS and $f_{c,corr}$, $\Delta\sigma_{corr}$ (Figures 7a and 7c), that suggest the linear correction, being a first order approximation, slightly overestimates the site effects for corner frequency and, thus, stress drop. The cc between the source parameters and the radiation pattern does not change significantly (from red solid curves to red dashed curves), as expected, and reassures us that the observed site effect biases and the correction (the blue curves) are not related to the assumed radiation patterns for these events.

The site-effect correction generally improves the consistency of the source parameters, as evidenced by the decrease in the standard deviation of the corner frequency and moment residuals (Figures 8a and 8b). Note that the standard deviation values are in logarithmic units. Estimates for events with fewer than 30 stations are less stable, suggesting ineffective corrections. The effectiveness of the correction on stress drop values is less obvious for individual events, but we note a decrease of the median standard deviation, indicating a bulk improvement (0.676–0.585; red lines in Figure 8c). The median standard deviations for corner frequency and moment decrease from 0.069 to 0.060 and from 0.019 to 0.018, respectively (red lines in Figures 8a and 8b). The site-effect-related standard deviation is 13% for corner frequency, 7% for the moment, and 13% for the stress drop. We estimate the site-effect-related variability to be 1.2 Hz and 0.16 MPa for an event with a corner frequency measurement of 30 Hz and a median stress drop of 2 MPa (Figure S9 and Text S5 in the Supporting Information S1).

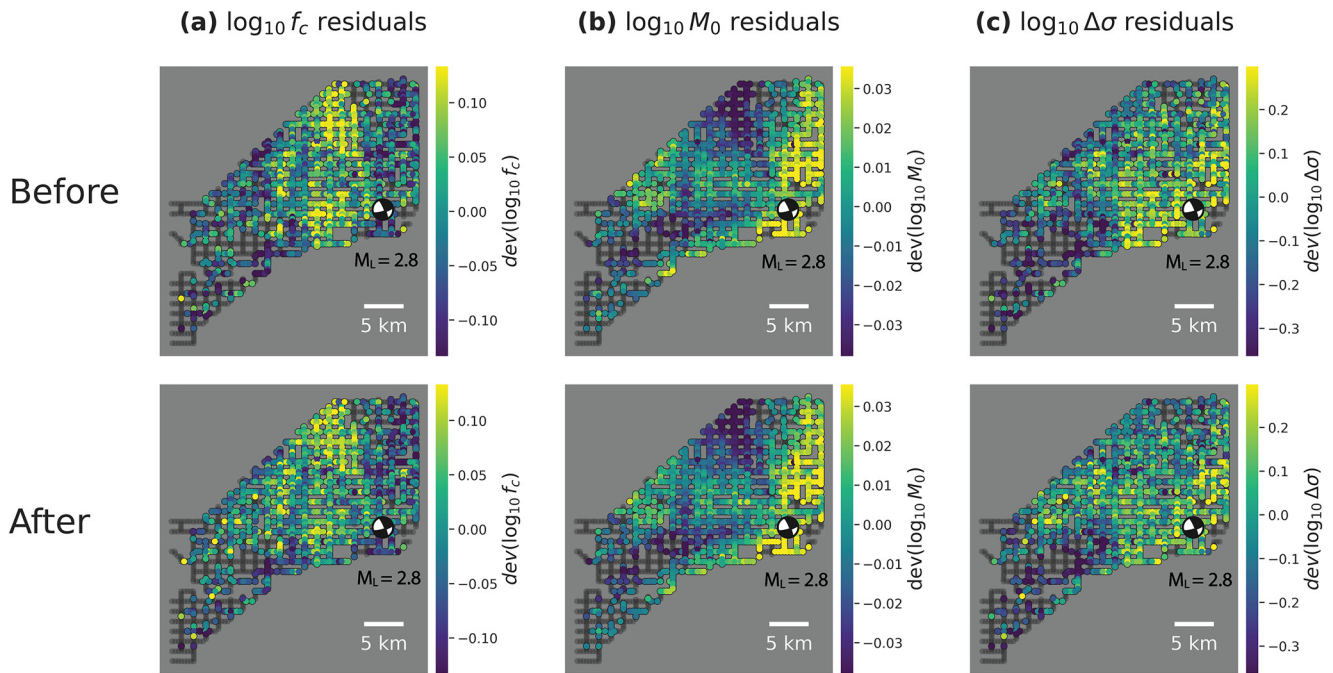


Figure 9. Comparison of the spatial distributions of the residuals of log-scaled (a) f_c , (b) M_0 , and (c) $\Delta\sigma$ before and after the site-effect corrections (Event 1 in Table S1 in Kemna et al., 2020). The focal mechanism is at the event location (at 6.05 km depth). The colorbar range is truncated at the pre-correction 5–95 percentiles. The correction uses site root-mean-square (RMS) in the S-wave window (10–30 s) at 10–15 Hz. The site-effect correction visibly reduces the spatial variability. The remaining variability of the source parameters for this event are likely associated with source directivity. The patterns are largely unclear for most other events (e.g., Figure S12 in the Supporting Information S1).

Overall, the site-effect-related deviations are consistent, but small. Despite the small site-effect deviations, the variability of source parameters decreases after the site-effect correction (Figure 9). Further, the corner frequency and stress drop estimates are more consistent after the correction (Figures 9a and 9c). The variation of moment for this event is clearly dominated by the focal mechanism (Figure 9b), which also appears to influence the remaining variation in corner frequencies (Figure 9a bottom). We note that we do not see a consistent similarity between the distribution of source parameters and the radiation pattern among events (the red distributions in Figure 7 centered around 0). We discuss the potential cause of the remaining variation in Section 6. We note that the median stress drop of all local events with more than 30 stations increases slightly after applying the site-effect correction (2.09–2.25 MPa; Figure S9 in the Supporting Information S1).

The standard deviations of source parameter residuals after correcting for site RMS are strongly dependent on the frequency band used, but are similar across the different phase time windows. The average post-correction standard deviation (Figure 10a) and the coefficient of variation of the correction term (Figure 10b) decreases for frequency bands from 2 to 21 Hz, with similar trends across the different phase time windows. Site corrections for the 15–21 Hz frequency band result in the lowest standard deviations for f_c and M_0 . In contrast, stress drop shows similar reductions in the standard deviation using site RMS corrections across frequency bands between 6 and 21 Hz. Thus, the frequency band of the site RMS correction that most strongly reduces the variability of both f_c and M_0 does not always result in as clear a reduction in the stress drop variability.

Figure 11 shows the behavior of the sub-arrays before and after the site-effect correction. The sub-arrays tend to produce higher corner frequency and stress drop values than the array median and the correction brings the trend down (Figures 11a and 11c). The higher estimated corner frequency suggests the assumed attenuation used in Kemna et al. (2020) might be higher than the array average (Ko et al., 2012). The site-effect correction, despite being small, corrects the moment and stress drop values closer to the average value (i.e., moving toward the $M_0/M_{0,true}$ and $\Delta\sigma/\Delta\sigma_{true} = 1$ lines in Figures 11b and 11c), suggesting improved spatial coherency. We find that the correction using site RMS at 10–15 Hz improves the stress drop coherency (Figure 11c) while correction using site RMS at 15–21 Hz decreases the coherency of stress drop despite increasing the coherency of corner frequency and moment (Figure S10 in the Supporting Information S1). Hence, site RMS at 10–15 Hz is a more effective site-effect proxy for obtaining consistent stress drop estimates.

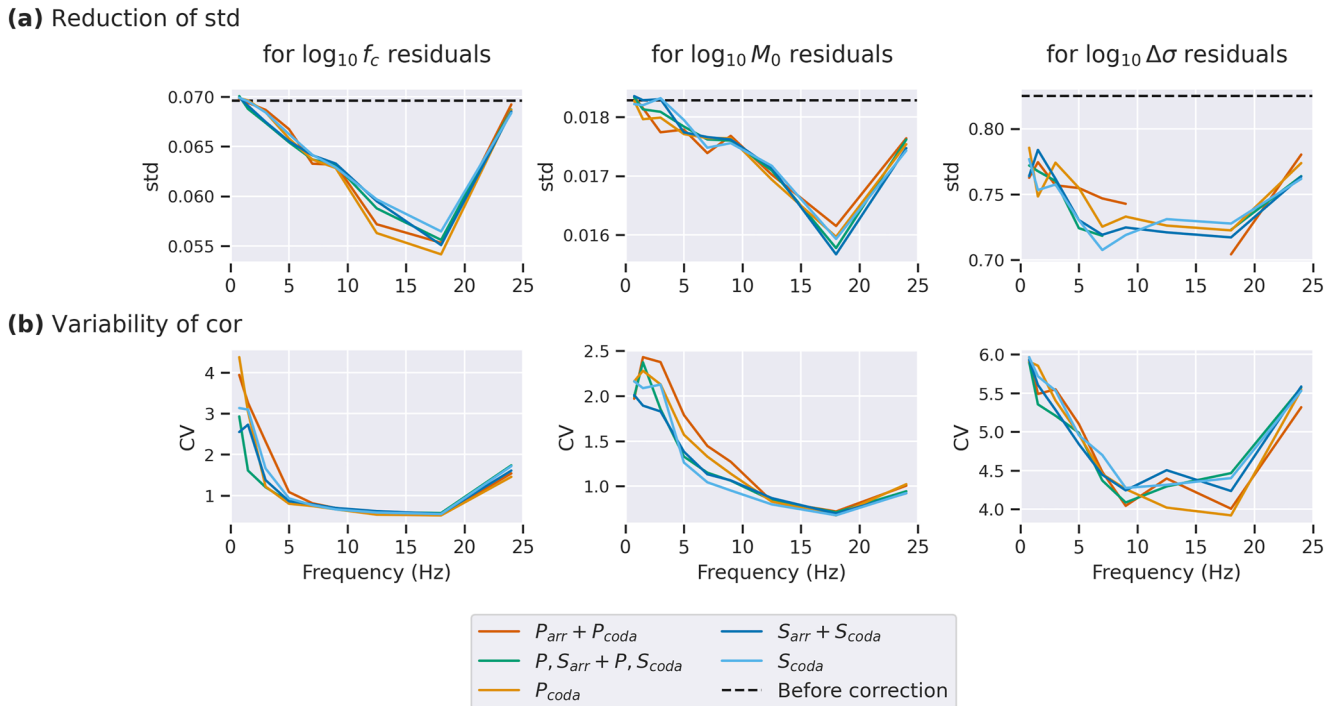


Figure 10. Comparison between the corrections using site root-mean-square (RMS) in a range of frequency bands and for different phase time windows (colors in the legend). (a) The standard deviation after correction (colored curves) for the residuals of log-scaled f_c , M_0 , and $\Delta\sigma$. The values plotted are the inter-event median standard deviation among the 906 events after correction. The dashed line marks the standard deviation before correction. Corrections using site RMS at the 10–15 Hz and 15–21 Hz frequency ranges are more effective in reducing the variability of source parameters. (b) The coefficient of variation (CV) of the correction term among the 906 events. The values plotted are the inter-station median CV of all stations (Equation 10). The smaller the CV, the lower variability of the correction terms on the stations across different events suggesting the corrections represent stationary site terms.

6. Discussion

In the first part of this study, we investigate site conditions across the LASSO array using the ground motion of regional earthquakes. We adjust ground motions for empirical geometric spreading and anelastic attenuation and solve for ground motions potentially related to source or site effects. The resulting ground motions exhibit significant variability. The amplitude variabilities are largest for the S-wave windows across all frequencies and for higher frequency (>10 Hz) P-wave windows (Figure 3). Roughly 5%–7% of the stations deviate by at least

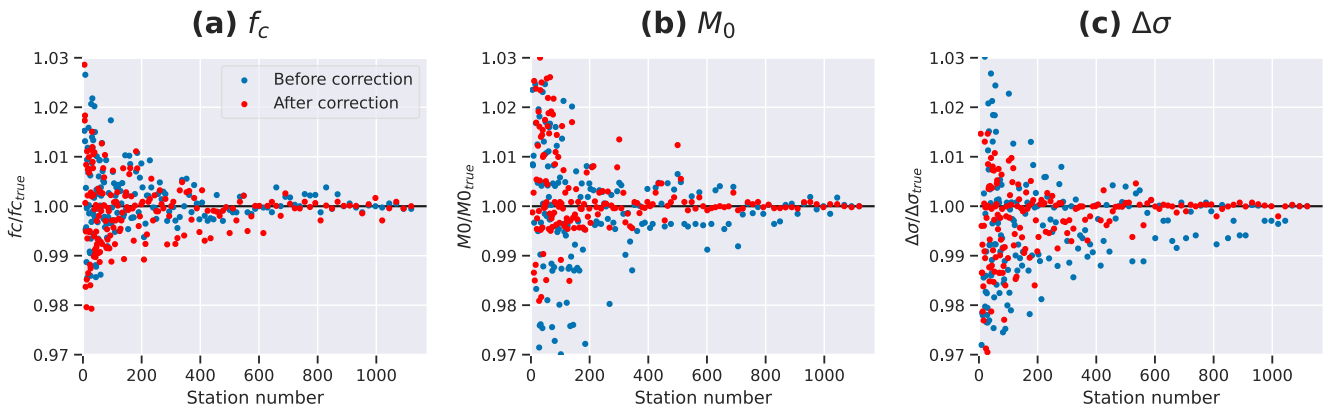


Figure 11. Deviations of source parameters (a) f_c , (b) M_0 , and (c) $\Delta\sigma$ obtained using a bootstrapping method with different number of stations in the sub-array. Each dot is the median of 100 randomly sampled sub-array of a given number of stations from one event (Event 1 in Table S1 in Kemna et al., 2020). For each sub-array, we calculate the median f_c , M_0 , and $\Delta\sigma$ and divide them by the median values of the entire array ($f_{c,true}$, $M_{0,true}$, and $\Delta\sigma_{true}$) to compare the deviation from the expected values. Blue and red dots use source parameters before and after the site-effect correction, respectively. The correction here uses site RMS in the S-wave window (10–30 s) at 10–15 Hz, improves the coherency of the stress drop (which is not the case for that at 15–21 Hz; see text).

100% from the median of the array, and 2%–3% deviate over 200% across the 40 km by 23 km area (Figure S5 in the Supporting Information S1). Johnson et al. (2020) found a 22% variation of the peak ground motions in an 0.6 km by 0.6 km small array across the San Jacinto Fault in California. In comparison, we observe larger ground motion deviation in LASSO likely because ground motions are examined across a larger area, and may also be affected by amplification of the alluvial sediments. We find the thin (8–30 m; Johnson & Luza, 2008) Quaternary sediments along major stream systems correspond to sites with high ground amplification (Figures 3d and 4). $V_{s,30}$ values estimated from topographic slope do not have a similar spatial distribution to the Quaternary units (Figure S1 in the Supporting Information S1) and correlate poorly with the observed ground motions (from 0.5 to 27 Hz; purple curves in Figure 4). The low correlation suggests topographic slopes in low relief regions such as LASSO (less than 150 m; Figure 2a) cannot accurately characterize $V_{s,30}$.

In the Central U.S., basin resonance also plays an important role in characterizing the ground motion (Goulet et al., 2018). The higher ground motions above 10 Hz toward the south west of the array (Figures 3a and 3b) match the dip direction of the Precambrian crystalline basement at 2.5 km depth (Crain & Chang, 2018). Despite the shallow basement dip (less than 1°; Crain & Chang, 2018), small changes in the thicknesses of the sediment layers can result in large local variations. The correspondence between larger ground motions and major river networks supports the results from a previous study that found higher ground water levels can amplify vertical ground motions (Liu & Tsai, 2018).

We observe the ground motions of regional earthquakes have progressively lower correlations with the P-wave radiation pattern with increasing frequency (Figure 4a left). This observation agrees with Trugman et al. (2021) who found a similar result by examining P arrivals of local earthquakes recorded by LASSO. They attributed the decreasing influence of radiation pattern at higher frequency to source complexity. Takemura et al. (2009) also found that amplitude variations associated with the S-wave radiation faded at high frequencies (>5 Hz) for a $M_w = 6.6$ regional earthquake in Japan. They suggested the loss of a discernible radiation pattern in the ground motions is caused by scattering due to crustal heterogeneity along the path. In our case, with longer time windows (11–20 s compared to 0.2 and 5 s in Takemura et al., 2009; Trugman et al., 2021), we interpret the loss of radiation pattern as being due to an increasing influence of surface geology (a site effect rather than a source or path effect). We also find the young sedimentary rocks and unconsolidated sediments amplify ground motions, resulting in positive cc between surface geology and site RMS. In the P-wave window, the amplification is observed mainly above 8 Hz (Figure 4a left) while in the S-wave window, the site amplification dominates across a larger range of frequencies (2–21 Hz; Figure 4a right). The high amplitude ground motions correlate with Pleistocene terrace deposits (Qt) at 2–4 Hz and shift to the youngest formation — the Holocene alluvium (Qal) — at increasing frequencies (Figure 3d), showing the depth sensitivity shifting to shallower layers in the subsurface with increasing frequency. A > 8 Hz amplification relates to a scale of less than 100 m near the surface (Al-Shukri et al., 1995).

We use site RMS in the S-wave window as a proxy for site effects. The lack of correlation between corner frequencies estimated using spectral-ratio methods and site RMS demonstrates the effectiveness of the spectral-ratio method at removing site effects (Figure 5b). The spectral-ratio approach makes no assumption about the attenuation and, therefore, is less subject to site effects (Ide et al., 2003). However, a good EGF is difficult to find in most cases. For EGF-related uncertainties and data selection criteria for reducing the uncertainties, we refer the interested readers to Abercrombie (2015). Corner frequencies estimated using single-spectral fitting method do appear to be influenced by site effects (Figure 5a). The negative correlation between corner frequency and site RMS (Figure 6a) is likely related to the attenuation effect of the soft sedimentary rocks and alluvium, which can have considerably low Q ($Q < 50$ in previous studies; Abercrombie, 1997) at local stations. The attenuation changes the spectral fall-off rate and has a tradeoff with the corner frequency measurements. The fitting uncertainty does not reflect this bias which has been demonstrated in Ko et al. (2012). Meanwhile, the amplification effect of the soft sedimentary layers and alluvium boosts the amplitude of the displacement spectra. The joint effect of a suppressed high frequency spectrum and a boosted low frequency plateau has been shown in literature comparing surface and borehole stations (e.g., Figure 4 in Abercrombie, 1997). The elevated spectral amplitudes result in positive correlation between seismic moment and site RMS (Figure 6b). The stress drops calculated using uncorrected M_0 and f_c parameters show a slightly negative correlation with site RMS, showing that site effects have an apparent bias on stress drop measurements across the LASSO array.

We capture the first order relationship between site effects and source parameters using a linear regression (Figure 6). We find the largest reduction in the variability of f_c and M_0 using corrections from the site RMS in the 15–21 Hz band (Figure 10a). However, the coherency of stress drops are not significantly improved (Figure S10

in the Supporting Information S1), suggesting the simple linear correction may result in over-correction. We find site RMS in the 10–15 Hz band improves the coherency of stress drops while reducing the biases in measured corner frequency and moment (Figure 11); hence, the 10–15 Hz band may provide a better proxy for site effects. The portion of the source property standard deviations that can be attributed to site effects are small (13%, 7%, and 13% for f_c , M_0 , and $\Delta\sigma$, respectively), in agreement with the relatively small travel time spent in the shallow layers and the overall minimal differences in shallow structure and topography across the LASSO array. We note that at least 30 or more stations are required to derive a reliable empirical relation to perform the site-effect correction. Linear relations estimated using fewer than 30 stations are unstable (Figure 6) and might increase the variability of source parameters (Figure 8).

Even after removing the site effect-related bias, the source parameters still show significant scatter (Figure 9, Figures S11 and S12 in the Supporting Information S1). The remaining variations might come from a few potential factors. The first factor is the attenuation of deeper structure (down to the basement at roughly 2 km; Johnson & Luza, 2008) as the ground motions we analyze are sensitive to only the top tens to at most a few hundreds of meters. However, if the change in sedimentary layer thickness is small as expected from the flat topography and the near-horizontal layers (K. S. Johnson & Luza, 2008) the effect is likely small. More work on local subsurface structure could verify the attenuation effect of the sedimentary layers. The second factor is the source directivity. We observe that some events exhibit similarities between the radiation pattern and source parameters (Figures 7a–7c); however, we find both positive and negative ccs and we only observe a high cc for a small number of events (Figure 7). The third factor is the model misfits due to an overly simplistic source model. Heterogeneous slip distributions may cause complex source spectra (e.g., Abercrombie, 2021). Thus, the uncertainty increases when fit with the Brune spectral model (Equation 2) that assumes a simple, circular fault. The source time functions of the event pairs we use in the spectral-ratio method show some earthquakes, despite being small, have complex rupture pulses (Figure S13 in the Supporting Information S1) that affect the spectral fits (Figures S14 and S15 in the Supporting Information S1). Ground motion analysis in Trugman et al. (2021) also suggested that our Events 15–17, along with other 21 local earthquakes they analyzed, have complex sources. Pennington et al. (2022) examined the source time functions of other events in the LASSO array and found complicated source pulses with multiple peaks. Hence, model misfit likely contributes significantly to the uncertainty of source parameters for local events like Events 15–17, where we do not observe significant correlation between source parameters and the source directivity (Figures S12, S14, and S15 in the Supporting Information S1).

To summarize, we find that site-effects may bias the measured source parameters. The site-effect biases are relatively small compared to the model misfit uncertainty, at least in a low-relief river plain similar to where LASSO was deployed. Having a dense station coverage around the source to capture the deviations due to source directivity and model misfit is of higher priority than having stations on different site conditions in a sedimentary plain like LASSO. Kemna et al. (2020) suggested that an increase from 10 to 20 stations can improve the 99.5% precision by three times for single-spectra estimates. Alternately, if few stations (<10) are available, minimizing azimuthal gaps can significantly reduce the uncertainty of stress drop. At sites with larger variation in topography, rock type (e.g., between hard rock and soft sediments), or basement depths, the amount of the bias due to site effects may be larger but further work could verify. Note that the site effect bias may be hard to quantify using our method in a typical network (usually <10 stations, nearly always <20 stations in regions of similar size).

7. Conclusions

We analyze the ground motions across the dense LARge-n Seismic Survey array in Oklahoma (LASSO) to quantify site effects and examine their relationship to source parameter estimates. The LASSO array is situated in a flat river plain (less than 150 m relief in a 40 km by 23 km area) with layered sedimentary rocks of Permian and Quaternary ages over a deep basement (2.5 km depth) gently dipping (less than 1°) to the south west. Despite the simple topography, the vertical ground motions of regional earthquakes (hypocentral distance 140–240 km) show significant variations that correspond to surface rock types and stream systems. Sites on Quaternary alluvial sediments can have ground motions that are three times larger than the array median. The site amplification is significant in the S-wave window from 2 to 21 Hz with spatial patterns likely reflecting the thickness of sedimentary layers and water content. In the P-wave window, the source radiation pattern dominates at low frequency (<4 Hz). The V_{s30} estimated based on topographic slope poorly correlates with the rock units and the observed

ground motions. We suggest that topographic slope alone is unlikely to accurately characterize the near-surface velocity in low relief regions like LASSO.

We find that the source parameters estimates for local earthquakes ($M_L < 3$) using the standard single-spectral fitting approach correlate with average ground motions of regional earthquakes at 10–15 Hz (site RMS). The corner frequency (f_c) negatively correlates ($cc = -0.5$) and seismic moment (M_0) positively correlates ($cc = 0.3$) with site RMS (Figure 6). The stress drop ($\Delta\sigma$) shows a negative correlation ($cc = -0.1$) with site RMS. The biases likely relate to the distortion of spectra caused by (a) high frequency attenuation and (b) an elevated low frequency plateau due to ground motions amplification by young, soft sedimentary rocks and alluvium. On the other hand, we show the spectral-ratio method can effectively remove the site-effect-related bias as expected (Figure 5b). We use a linear regression to estimate the first-order influence of site effects and correct the biased source parameters, which reduces 13%, 7%, and 13% of the standard deviation for the measured corner frequency, moment, and stress drop, respectively. We find a minimum of 30 stations is required to get a stable site-effect estimate and improves the spatial coherency of the target source parameters (Figures 6 and 8).

The weak-to-moderate but statistically significant correlation between ground motions and source parameters implies the site effects affect the source parameter estimates, but other important influences also exist. Factors that may contribute to the variability include (a) attenuation of deeper sedimentary layers (0.1–2 km), (b) source directivity, and (c) model misfit due to using an over-simplified source model. The uncertainty from model misfit is likely the main contributor of the variability, supported by the complex source time functions and other studies in this region (Pennington et al., 2022; Trugman et al., 2021). Even small magnitude earthquakes ($M_L = 0.01$ –3) can have complex ruptures that produce source spectra more complicated than assumed by the simple, circular source model (Figure S13 in the Supporting Information S1). Some events also show significant influence from source directivity. A more detailed mapping of the subsurface structure underneath the LASSO array could help verify the attenuation of the sedimentary layers and explain the observed ground motion patterns (Figure 3). Site effects are expected to play a larger role in regions with more strongly varying topography, rock types, and depth to basement, which could be investigated in the future. If three-component data are available, using the H/V ratio to quantify site effects and compare with site effects estimated by our methodology could also be valuable.

Data Availability Statement

The earthquake waveform data used in this study are openly available at the International Federation of Digital Seismograph Networks (FDSN) (Dougherty et al., 2016). The local events catalogs and focal mechanisms are from Cochran, Wickham-Piotrowski, et al. (2020) and Trugman et al. (2021). The regional events catalogs and focal mechanisms are downloaded from Earthquake Hazards Program Advanced National Seismic System (ANSS) Comprehensive Catalog of Earthquake Events and Products (U.S. Geological Survey, 2022). The Oklahoma river and stream system maps are downloaded from the Oklahoma Water Resources Board Open Data (Oklahoma Water Resources Board, 2022). The V_{s30} are available on the U.S. Geological Survey Earthquake Hazards Program V_{s30} Map (Yong et al., 2016). The authors use Obspy (Beyreuther et al., 2010) to process the seismograms and plot the local maps. The authors use PyGMT (Uieda et al., 2022) and GMT (Wessel et al., 2019) to plot the regional maps and download the Earth relief data from the National Aeronautics and Space Administration (NASA) (NASA JPL, 2013). The authors use LMFIT (Newville et al., 2016) to perform the regression analysis and fit the spectra. The authors use Pykonal (White et al., 2020) to calculate the earthquake ray path in Figure S16 in the Supporting Information S1.

References

- Abercrombie, R. E. (1995). Earthquake source scaling relationships from 1 to 5 ML using seismograms recorded at 2.5 km depth. *Journal of Geophysical Research*, 100(B12), 24015–24036. <https://doi.org/10.1029/95jb02397>
- Abercrombie, R. E. (1997). Near-surface attenuation and site effects from comparison of surface and deep borehole recordings. *Bulletin of the Seismological Society of America*, 87(3), 731–744. <https://doi.org/10.1785/bssa0870030731>
- Abercrombie, R. E. (2014). Stress drops of repeating earthquakes on the San Andreas fault at parkfield. *Geophysical Research Letters*, 41(24), 8784–8791. <https://doi.org/10.1002/2014gl062079>
- Abercrombie, R. E. (2015). Investigating uncertainties in empirical green's function analysis of earthquake source parameters. *Journal of Geophysical Research: Solid Earth*, 120(6), 4263–4277. <https://doi.org/10.1002/2015jb011984>
- Abercrombie, R. E. (2021). Resolution and uncertainties in estimates of earthquake stress drop and energy release. *Philosophical Transactions of the Royal Society A*, 379, 20200131. <https://doi.org/10.1098/rsta.2020.0131>

Acknowledgments

The authors thank D. Kilb and A. Baltay, an anonymous reviewer, and the Editor, S. Ide for their reviews and comments that significantly improved the manuscript. This research was supported by the U.S. Geological Survey under Grant G20AP00022, G20AP00023, G22AP00012, and G22AP00035 to Massachusetts Institute of Technology and Boston University. This work was performed under the auspices of the U.S. Department of Energy by Lawrence Livermore National Laboratory under Contract DE-AC52-07NA27344. Any use of trade, firm, or product names is for descriptive purposes only and does not imply endorsement by the U.S. Government.

- Abercrombie, R. E., Bannister, S., Ristau, J., & Doser, D. (2016). Variability of earthquake stress drop in a subduction setting, the Hikurangi margin, New Zealand. *Geophysical Journal International*, 208, 306–320. <https://doi.org/10.1093/gji/ggw393>
- Allmann, B. P., & Shearer, P. M. (2009). Global variations of stress drop for moderate to large earthquakes. *Journal of Geophysical Research*, 114(B1), B01310. <https://doi.org/10.1029/2008jb005821>
- Al-Shukri, H. J., Pavlis, G. L., & Vernon, F. L., III. (1995). Site effect observations from broadband arrays. *Bulletin of the Seismological Society of America*, 85(6), 1758–1769. <https://doi.org/10.1785/BSSA0850061758>
- Anderson, J. G., & Hough, S. E. (1984). A model for the shape of the Fourier amplitude spectrum of acceleration at high frequencies. *Bulletin of the Seismological Society of America*, 74(5), 1969–1993. <https://doi.org/10.1785/BSSA0740051969>
- Beyreuther, M., Barsch, R., Krischer, L., Megies, T., Behr, Y., & Wassermann, J. (2010). ObsPy: A python toolbox for seismology [Software]. *Seismological Research Letters*, 81, 530–533. <https://doi.org/10.1785/gssrl.81.3.530>
- Boatwright, J. (1978). Detailed spectral analysis of two small new york state earthquakes. *Bulletin of the Seismological Society of America*, 68(4), 1117–1131. <https://doi.org/10.1785/BSSA0680041117>
- Boatwright, J. (1980). A spectral theory for circular seismic sources; simple estimates of source dimension, dynamic stress drop, and radiated seismic energy. *Bulletin of the Seismological Society of America*, 70(1), 1–27. <https://doi.org/10.1785/BSSA0700010001>
- Boore, D. M. (2003). Simulation of ground motion using the stochastic method. *Pure and Applied Geophysics*, 160, 635–676. <https://doi.org/10.1007/pl00012553>
- Boore, D. M., & Boatwright, J. (1984). Average body-wave radiation coefficients. *Bulletin of the Seismological Society of America*, 74(5), 1615–1621. <https://doi.org/10.1785/bssa0740051615>
- Boore, D. M., Joyner, W. B., & Fumal, T. E. (1993). *Estimation of response spectra and peak accelerations from western north american earthquakes: An interim report* (technical report no. Open-file report 93-509). U.S. Geological Survey. <https://doi.org/10.3133/ofr93509>
- Boore, D. M., Stewart, J. P., Seyhan, E., & Atkinson, G. M. (2014). NGA-West2 equations for predicting PGA, PGV, and 5% damped PSA for shallow crustal earthquakes. *Earthquake Spectra*, 30(3), 1057–1085. <https://doi.org/10.1193/070113EQS18>
- Borcherdt, R. D. (1970). Effects of local geology on ground motion near san francisco bay. *Bulletin of the Seismological Society of America*, 60(1), 29–61. <https://doi.org/10.1785/BSSA0600010029>
- Borcherdt, R. D. (1994). Estimates of site-dependent response spectra for design (methodology and justification). *Earthquake Spectra*, 10(4), 617–653. <https://doi.org/10.1193/1.1585791>
- Brune, J. N. (1970). Tectonic stress and the spectra of seismic shear waves from earthquakes. *Journal of Geophysical Research*, 75(26), 4997–5009. <https://doi.org/10.1029/jb075i026p04997>
- Building Seismic Safety Council (2020). *NEHRP recommended seismic provisions for new buildings and other structures* (technical report no. FEMA P-2082-1). Federal Emergency Management Agency.
- Cochran, E. S., Wickham-Piotrowski, A., Kemna, K. B., Harrington, R. M., Dougherty, S. L., & Peña Castro, A. F. (2020). Minimal clustering of injection-induced earthquakes observed with a large-n seismic array. *Bulletin of the Seismological Society of America*, 110(5), 2005–2017. <https://doi.org/10.1785/0120200101>
- Cochran, E. S., Wolin, E., McNamara, D. E., Yong, A., Wilson, D., Alvarez, M., et al. (2020). The U.S. geological survey's rapid seismic array deployment for the 2019 ridgecrest earthquake sequence. *Seismological Research Letters*, 91(4), 1952–1960. <https://doi.org/10.1785/0220190296>
- Crain, K. D., & Chang, J. C. (2018). Elevation map of the top of the crystalline basement in Oklahoma and surrounding states. *Oklahoma Geological Survey Open-File Report OF1-2018*.
- Dougherty, S. L., Cochran, E. S., & Harrington, R. M. (2016). LArge-n seismic survey in Oklahoma [Dataset]. International federation of digital Seismograph Networks. https://doi.org/10.7914/SN/2A_2016
- Dougherty, S. L., Cochran, E. S., & Harrington, R. M. (2019). The large-N seismic survey in Oklahoma (LASSO) experiment. *Seismological Research Letters*, 90(5), 2051–2057. <https://doi.org/10.1785/0220190094>
- Eshelby, J. D. (1957). The determination of the elastic field of an ellipsoidal inclusion, and related problems. *Proceedings of the Royal Society of London — Series A: Mathematical and Physical Sciences*, 241(1226), 376–396. <https://doi.org/10.1098/rspa.1957.0133>
- Field, E. H., Johnson, P. A., Beresnev, I. A., & Zeng, Y. (1997). Nonlinear ground-motion amplification by sediments during the 1994 northridge earthquake. *Nature*, 390(6660), 599–602. <https://doi.org/10.1038/37586>
- Goulet, C. A., Bozorgnia, Y., Abrahamson, N. A., Kuehn, N., Al Atik, L., Youngs, R. R., et al. (2018). *Central and eastern north America ground-motion characterization (NGA-East)*. (technical Report). University of California.
- Hartzell, S. H. (1978). Earthquake aftershocks as green's functions. *Geophysical Research Letters*, 5(1), 1–4. <https://doi.org/10.1029/g1005i001p00001>
- Hauksson, E., Yoon, C., Yu, E., Andrews, J. R., Alvarez, M., Bhadha, R., & Thomas, V. (2020). Caltech/USGS southern california seismic network (SCSN) and southern california earthquake data center (SCEDC): Data availability for the 2019 ridgecrest sequence. *Seismological Research Letters*, 91(4), 1961–1970. <https://doi.org/10.1785/0220190290>
- Heran, W. D., Green, G. N., & Stoesser, D. B. (2003). *A digital geologic map database for the state of Oklahoma* (technical report). U.S. Geological Survey.
- Holland, A. A. (2013). Optimal fault orientations within Oklahoma. *Seismological Research Letters*, 84(5), 876–890. <https://doi.org/10.1785/0220120153>
- Hough, S. (1997). Empirical green's function analysis: Taking the next step. *Journal of Geophysical Research*, 102(B3), 5369–5384. <https://doi.org/10.1029/96jb03488>
- Huang, Y., Ellsworth, W. L., & Beroza, G. C. (2017). Stress drops of induced and tectonic earthquakes in the central United States are indistinguishable. *Science Advances*, 3(8), e1700772. <https://doi.org/10.1126/sciadv.1700772>
- Ide, S., Beroza, G. C., Prejean, S. G., & Ellsworth, W. L. (2003). Apparent break in earthquake scaling due to path and site effects on deep borehole recordings. *Journal of Geophysical Research*, 108(B5), 2271. <https://doi.org/10.1029/2001jb001617>
- Johnson, C. W., Kilb, D., Baltay, A., & Vernon, F. (2020). Peak ground velocity spatial variability revealed by dense seismic array in southern California. *Journal of Geophysical Research: Solid Earth*, 125(6), e2019JB019157. <https://doi.org/10.1029/2019jb019157>
- Johnson, K. S., & Luza, K. V. (2008). *Earth sciences and mineral resources of Oklahoma*. Oklahoma Geological Survey.
- Kane, D. L., Prieto, G. A., Vernon, F. L., & Shearer, P. M. (2011). Quantifying seismic source parameter uncertainties. *Bulletin of the Seismological Society of America*, 101(2), 535–543. <https://doi.org/10.1785/0120100166>
- Kaneko, Y., & Shearer, P. (2014). Seismic source spectra and estimated stress drop derived from cohesive-zone models of circular subshear rupture. *Geophysical Journal International*, 197(2), 1002–1015. <https://doi.org/10.1093/gji/ggu030>
- Kaneko, Y., & Shearer, P. (2015). Variability of seismic source spectra, estimated stress drop, and radiated energy, derived from cohesive-zone models of symmetrical and asymmetrical circular and elliptical ruptures. *Journal of Geophysical Research: Solid Earth*, 120(2), 1053–1079. <https://doi.org/10.1002/2014jb011642>

- Kemna, K., Peña Castro, A., Harrington, R., & Cochran, E. S. (2020). Using a large-n seismic array to explore the robustness of spectral estimations. *Geophysical Research Letters*, 47(21), e2020GL089342. <https://doi.org/10.1029/2020gl089342>
- Kilb, D., Biasi, G., Anderson, J., Brune, J., Peng, Z., & Vernon, F. L. (2012). A comparison of spectral parameter kappa from small and moderate earthquakes using southern California ANZA seismic network data. *Bulletin of the Seismological Society of America*, 102(1), 284–300. <https://doi.org/10.1785/0120100309>
- Ko, Y.-T., Kuo, B.-Y., & Hung, S.-H. (2012). Robust determination of earthquake source parameters and mantle attenuation. *Journal of Geophysical Research*, 117(B4), B04304. <https://doi.org/10.1029/2011jb008759>
- Ktenidou, O.-J., Cotton, F., Abrahamson, N. A., & Anderson, J. G. (2014). Taxonomy of κ : A review of definitions and estimation approaches targeted to applications. *Seismological Research Letters*, 85(1), 135–146. <https://doi.org/10.1785/0220130027>
- Kwiatek, G., Bulut, F., Bohnhoff, M., & Dresen, G. (2014). High-resolution analysis of seismicity induced at Berlín geothermal field, El Salvador. *Geothermics*, 52, 98–111. <https://doi.org/10.1016/j.geothermics.2013.09.008>
- Liu, H.-W., & Tsai, C.-C. (2018). Site effect of vertical motion amplification behavior observed from downhole arrays. *Journal of GeoEngineering*, 13(1), 39–48. [https://doi.org/10.6310/jog.2018.13\(1\).4](https://doi.org/10.6310/jog.2018.13(1).4)
- Madariaga, R. (1976). Dynamics of an expanding circular fault. *Bulletin of the Seismological Society of America*, 66(3), 639–666. <https://doi.org/10.1785/bssa0660030639>
- Mori, J., & Frankel, A. (1990). Source parameters for small events associated with the 1986 North palm springs, California, earthquake determined using empirical green functions. *Bulletin of the Seismological Society of America*, 80(2), 278–295. <https://doi.org/10.1785/bssa0800030507>
- Nakamura, Y. (1989). A method for dynamic characteristics estimation of subsurface using microtremor on the ground surface. *Railway Technical Research Institute, Quarterly Reports*, 30, Retrieved from https://www.sdr.co.jp/papers/hv_1989.pdf
- NASA JPL. (2013). National aeronautics and space administration (NASA) shuttle radar topography mission global 1 arc second [Dataset]. NASA EOSDIS Land Processes DAAC. <https://doi.org/10.5067/MEaSUREs/SRTM/SRTMGL1.003>
- Neighbors, C., Cochran, E. S., Ryan, K., & Kaiser, A. E. (2017). Solving for source parameters using nested array data: A case study from the Canterbury, New Zealand earthquake sequence. *Pure and Applied Geophysics*, 174(3), 875–893. <https://doi.org/10.1007/s00024-016-1445-2>
- Newville, M., Stensitzki, T., Allen, D. B., Rawlik, M., Ingarigiola, A., & Nelson, A. (2016). LMFIT: Non-linear least-square minimization and curve-fitting for python [Software]. Astrophysics Source Code Library. Retrieved from 2016ascl.soft06014N
- Oklahoma Water Resources Board (2022). Surface water data [Dataset]. Oklahoma Water Resources Board. Retrieved from <https://home-owrb.opendata.arcgis.com/data%20sets?t=surface>
- Pennington, C. N., Chang, H., Rubinstein, J. L., Abercrombie, R. E., Nakata, N., Uchide, T., & Cochran, E. S. (2022). Quantifying the sensitivity of microearthquake slip inversions to station distribution using a dense nodal array. *Bulletin of the Seismological Society of America*, 112, 1252–1270. <https://doi.org/10.1785/0120210279>
- Pennington, C. N., Chen, X., Abercrombie, R. E., & Wu, Q. (2021). Cross validation of stress drop estimates and interpretations for the 2011 prague, OK, earthquake sequence using multiple methods. *Journal of Geophysical Research: Solid Earth*, 126(3), e2020JB020888. <https://doi.org/10.1029/2020jb020888>
- Shearer, P. M. (2019). *Introduction to seismology*. Cambridge university press.
- Shearer, P. M., Abercrombie, R. E., Trugman, D. T., & Wang, W. (2019). Comparing EGF methods for estimating corner frequency and stress drop from P wave spectra. *Journal of Geophysical Research: Solid Earth*, 124(4), 3966–3986. <https://doi.org/10.1029/2018jb016957>
- Shearer, P. M., Prieto, G. A., & Hauksson, E. (2006). Comprehensive analysis of earthquake source spectra in southern California. *Journal of Geophysical Research*, 111(B6), B06303. <https://doi.org/10.1029/2005jb003979>
- Sonley, E., Abercrombie, R. E., & Abercrombie, R. (2006). Effects of methods of attenuation correction on source parameter determination. *Geophysical Monograph-American Geophysical Union*, 170, 91–97. <https://doi.org/10.1029/170gm11>
- Taira, T., Abercrombie, R., & Baltay, A. (2021). Introduction to the SCEC Community stress drop validation study. *Agü fall meeting abstracts*, 2021, S45A–0282. Retrieved from <https://ui.adsabs.harvard.edu/abs/2021AGUFM.S45A0282T/abstract>
- Takemura, S., Furumura, T., & Saito, T. (2009). Distortion of the apparent S-wave radiation pattern in the high-frequency wavefield: Tottori-Ken Seibu, Japan, earthquake of 2000. *Geophysical Journal International*, 178(2), 950–961. <https://doi.org/10.1111/j.1365-246x.2009.04210.x>
- Trugman, D. T., Chu, S. X., & Tsai, V. C. (2021). Earthquake source complexity controls the frequency dependence of near-source radiation patterns. *Geophysical Research Letters*, 48(17), e2021GL095022. <https://doi.org/10.1029/2021gl095022>
- Uieda, L., Tian, D., Leong, W. J., Jones, M., Schlitzer, W., Grund, M., et al. (2022). PyGMT: A Python interface for the generic mapping tools [Software]. Zenodo. <https://doi.org/10.5281/zenodo.6702566>
- U.S. Geological Survey. (2022). Earthquake hazards program advanced national seismic system (ANSS) comprehensive catalog of earthquake events and products: Catalog (m > 3) in central Oklahoma (2016-04-14–2016-05-10) [Dataset]. U.S. Geological Survey. Retrieved from <https://earthquake.usgs.gov/earthquakes/map/?extent=33.96842,-98.70667&extent=35.93132,-95.02625&range=search&-timeZone=utc&search=%7B%22name%22:%22Search%20Results%22,%22params%22:%7B%22starttime%22:%222016-04-14%2000:00:00%22,%22endtime%22:%222016-05-10%2023:59:59%22,%22maxlatitude%22:35.8,%22minlatitude%22:34.103,%22maxlongitude%22:-95.208,%22minlongitude%22:-98.525,%22minmagnitude%22:3,%22orderby%22:%22time%22%7D%7D>
- Viegas, G., Abercrombie, R. E., & Kim, W.-Y. (2010). The 2002 M5 Au sable forks, NY, earthquake sequence: Source scaling relationships and energy budget. *Journal of Geophysical Research*, 115(B7), B07310. <https://doi.org/10.1029/2009jb006799>
- Wald, D. J., & Allen, T. I. (2007). Topographic slope as a proxy for seismic site conditions and amplification. *Bulletin of the Seismological Society of America*, 97(5), 1379–1395. <https://doi.org/10.1785/0120060267>
- Wessel, P., Luis, J., Uieda, L., Scharroo, R., Wobbe, F., Smith, W. H., & Tian, D. (2019). The generic mapping tools version 6 [Software]. *Geochemistry, Geophysics, Geosystems*, 20, 5556–5564. <https://doi.org/10.1029/2019gc008515>
- White, M. C., Fang, H., Nakata, N., & Ben-Zion, Y. (2020). PyKonal: A python package for solving the eikonal equation in spherical and cartesian coordinates using the fast marching method [Software]. *Seismological Research Letters*, 91, 2378–2389. <https://doi.org/10.1785/0220190318>
- Yong, A., Hough, S. E., Iwahashi, J., & Braverman, A. (2012). A terrain-based site-conditions map of California with implications for the contiguous United States. *Bulletin of the Seismological Society of America*, 102(1), 114–128. <https://doi.org/10.1785/0120100262>
- Yong, A., Thompson, E. M., Wald, D. J., Knudsen, K. L., Odum, J. K., Stephenson, W. J., & Haefner, S. (2016). *Compilation of V_{s30} data for the United States* (Technical Report) [Dataset]. U.S. Geological Survey. Retrieved from <https://pubs.er.usgs.gov/publication/ds978>